Gene regulatory network inference in soybean upon infection by *Phytophthora sojae*

Brett Hale[1,2,3,¶], Sandaruwan Ratnayake[2,3,¶,#a], Ashley Flory[2,#b], Ravindu Wijeratne[4], Clarice Schmidt[5], Alison E. Robertson[5], and Asela J. Wijeratne[2,3,*]

[1]Molecular Biosciences Graduate Program, Arkansas State University, State University, AR, USA

[2]Arkansas Biosciences Institute, Arkansas State University, State University, AR, USA

[3]College of Science and Mathematics, Arkansas State University, State University, AR, USA

[4]Houston High School, Germantown, TN, USA

[5]Department of Plant Pathology and Microbiology, Iowa State University, Ames, IA, USA

[¶]These authors contributed equally to this work.

[#a]Current address: Donald Danforth Plant Science Center, St. Louis, MO, USA

[#b]Current address: St. Jude Children's Research Hospital, Memphis, TN, USA

*Corresponding author
E-mail: awijeratne@astate.edu

Short title: Plant immunity and gene regulatory networks

Abstract

Phytophthora sojae is a soil-borne oomycete and the causal agent of Phytophthora root and stem rot (PRR) in soybean (*Glycine max* [L.] Merrill). Yield losses attributed to *P. sojae* are devastating in disease-conducive environments, with global estimates surpassing 1.1 million tonnes annually. Historically, management of PRR has entailed host genetic resistance (both vertical and horizontal) complemented by disease-suppressive cultural practices (e.g., oomicide application). However, the vast expansion of complex and/or diverse *P. sojae* pathotypes necessitates developing novel technologies to attenuate PRR in field environments. Therefore, the objective of the present study was to couple high-throughput sequencing data and deep learning to elucidate molecular features in soybean following infection by *P. sojae*. In doing so, we generated transcriptomes to identify differentially expressed genes (DEGs) during compatible and incompatible interactions with *P. sojae* and a mock inoculation. The expression data were then used to select two defense-related transcription factors (TFs) belonging to WRKY and RAV families. DNA Affinity Purification and sequencing (DAP-seq) data were obtained for each TF, providing putative DNA binding sites in the soybean genome. These bound sites were used to train Deep Neural Networks with convolutional and recurrent layers to predict new target sites of WRKY and RAV family members in the DEG set. Moreover, we leveraged publicly available Arabidopsis (*Arabidopsis thaliana*) DAP-seq data for five TF families enriched in our transcriptome analysis to train similar models. These Arabidopsis data-based models were used for cross-species TF binding site prediction on soybean. Finally, we created a gene regulatory network depicting TF-target gene interactions that orchestrate an immune response against *P. sojae*. Information herein provides novel insight into molecular plant-pathogen interaction and may prove useful in developing soybean cultivars with more durable resistance to *P. sojae*.

Keywords: soybean, *P. sojae*, transcription factor, gene regulation, gene regulatory network, deep learning

Author Summary

Global food security is threatened continually by plant pathogens. One approach to circumvent these disease-causing agents entails understanding how hosts balance primary growth and defense upon pathogen perception. Molecular signatures of perception-rendered defense may be leveraged subsequently to develop resistant/tolerant crop plants. Additionally, evidence suggests that the plant immune system is characterized by tuning primary and secondary metabolic activity via transcription factor-mediated transcriptional reprogramming. Therefore, we investigated transcription factor-target gene interactions in soybean upon infection by compatible and incompatible races of *Phytophthora sojae*. Through transcriptome analysis, we found that the interactions elicited vast, overlapping transcriptional responses and identified overrepresented, defense-related transcription factor families. We then generated/acquired DNA-protein interactome data for the most represented transcription factor families in the transcriptome analysis and trained deep learning-based models to predict novel transcription factor targets. Transcription factor/target gene metrics were used to construct a gene regulatory network with prioritized components. We identified hub transcription factors belonging to WRKY and ERF families, the majority of which function in response to various biotic and abiotic stressors. These findings propose novel regulators in the soybean defense response to *Phytophthora sojae* and provide an avenue for the investigation of transcription factor-target gene interactions in plants.

Introduction

Phytophthora sojae Kaufmann and Gerdemann is a hemibiotrophic, homothallic oomycete that renders significant yield losses in soybean (*Glycine max* [L.] Merrill). The pathogen can infect host plants at any developmental stage and is denoted by damping-off in seedlings (early season) as well as root rot and subsequent chlorosis/necrosis in aboveground tissue (late season) [1]. In addition, *P. sojae* oospores can persist in a production environment for several years, limiting the efficacy of most cultural management strategies [2,3]. Thus, the most economical and environmentally benign method to manage the pathogen is the deployment of horizontal and/or vertical host genetic resistance [4]. Horizontal resistance is quantitatively inherited and provides some level of protection against all *P. sojae* pathotypes. However, early-season efficiency is reliant upon complementation with cultural practices [3] as it is only active after the first true leaf stage. Moreover, the polygenic character of horizontal resistance hinders introgression into germplasm [5,6]. Alternatively, vertical resistance (i.e., incompatibility) embodies the classic gene-for-gene concept and renders complete protection against specific pathotypes in a monogenic manner [7]. The selective pressures imposed by vertically resistant soybean have increased the virulence profile of *P. sojae* populations, restricting the use of cultivars with a specific *Resistance to P. sojae* (*Rps*) gene to 8-15 years [2,8]. Therefore, a deeper understanding of the molecular mechanisms governing soybean defense against *P. sojae* is needed to overcome pathogen evolution and ultimately attenuate disease.

During a compatible (virulent) soybean-*P. sojae* interaction, the host plant perceives microbe-associated molecular patterns (MAMPs)/pathogen-associated molecular patterns (PAMPs) and elicits PAMP-triggered immunity (PTI), a basal immune response effective against non-adapted pathogens [9]. Conversely, *P. sojae* secretes *Avirulence* (*Avr*) gene-encoded effector proteins that suppress components of PTI and promote disease. During incompatibility, a receptor

encoded by an *Rps* gene recognizes the cognate *Avr* gene product and activates effector-triggered immunity (ETI), a hypersensitive immune response that potentiates PTI and confers resistance to *P. sojae* [7,9,10]. The combined efforts of PTI and ETI to mitigate disease during incompatibility exemplify the zig-zag model of Jones and Dangl [11] and portray PTI and ETI as distinct events that occur consecutively. A growing body of evidence obscures these boundaries, particularly in plant-*Phytophthora* interactions, instead suggesting that plant defense spans a PTI:ETI continuum [12,13]. For these reasons, Wang et al. [14] proposed a three-layered model of plant immunity comprising a recognition layer, a signal-integration layer, and a defense-action layer. In the context of soybean-*P. sojae* interaction, our understanding of the signal-integration layer remains the most fragmented.

Intra- and/or extracellular pathogen perception triggers a dynamic, highly sophisticated signaling network that balances primary and secondary metabolic activity in a manner preservative of host fitness [15]. Signal integration and convergence accompanying this coordinated stress response are mediated by transcription factors (TFs) and transcriptional cofactors that comprise sensory regulatory networks embedded within phytohormone signaling pathways [16,17]. Dynamism and amplification of such networks are determined by physical interaction between TFs and nucleocytoplasmic receptors [18,19], TF phosphorylation by mitogen-activated protein kinase (MAPK) cascades [20], and feedback regulation of Ca^{2+} signaling, among other mechanisms [17]. While the abundance and diversity of TFs required for immunity vary across plant species and pathosystems [21], elucidated sensory regulatory networks tend to possess members of the bHLH, bZIP, ERF, MYB, NAC, and WRKY families [17,22,23] that collectively direct transcriptional reprogramming of downstream target genes [16]. Isolated studies have evidenced transcriptional reprogramming in soybean upon infection by *P. sojae* [24,25,26,27] and

117 have identified various TFs associated with defense [28,29,30,31,32,33,34,35,36,37]; yet
118 mechanistic insight regarding TF-target gene interactions and their organization within larger
119 hierarchical networks is lacking. This systems-level information can be unraveled using gene
120 regulatory networks (GRNs) [38], and regulatory hubs identified subsequently through analyses
121 of network tunability and redundancy [21].

122 In a simplistic model of gene regulation, TFs bind to regulatory DNA motifs in target genes
123 to modulate transcriptional activity [39]. GRNs can be used to discern static and spatiotemporal
124 interactions between TFs and DNA motifs as well as interaction abundance, topology, and
125 influence on target gene expression [40,41]. Various experimental and computational methods
126 have been developed to study gene regulation and function for a phenomenon of interest (e.g.,
127 disease resistance) [38]. As an example, TF-DNA interactome approaches such as chromatin
128 immunoprecipitation followed by sequencing (ChIP-seq) and DNA-affinity purification and
129 sequencing (DAP-seq) allow the identification of many TF binding sites at once and can be used
130 to validate interactions inferred by gene expression analysis [41,42]. However, these
131 methodologies are technically- and economically-demanding and are thus difficult to deploy at
132 genome-scale.

133 Contrarily, *in silico* exploration of TF-target interactions is easily scalable. The majority of
134 such methods leverage guilt-by-association approaches that cannot necessarily predict causality
135 and are thus limited in terms of elucidating regulatory pathways [43]. One can overcome this by
136 using a bottom-up approach to identify *cis*-regulatory elements (CREs), which modulate gene
137 expression by recruiting TFs, as a means to presume TF-target gene interactions. The most popular
138 approach to find CREs is to employ a supervised motif method using a position-specific score
139 matrix (i.e., position weight matrix) and map CREs to a promoter [44]. However, given that CREs

140 are often degenerate and short, this method suffers from high false positive rates. Improvement
141 can be made by considering the evolutionary conservation of CREs (albeit all functional CREs are
142 not necessarily evolutionary conserved) or gene co-regulation. More recently, Deep Neural
143 Network (DNN)-based methods were developed to detect TF binding sites (TFBS) [45,46]. The
144 DNN-based techniques are deemed superior to others given their ability to accept minor CRE
145 variation and sequence context surrounding TFBS and thus transfer across species [47]. For
146 instance, leveraging Arabidopsis (*Arabidopsis thaliana*) cistrome datasets, Akagi et al. [48]
147 constructed convolutional neural network (CNN)-based DNN models for cross-species prediction
148 of TFBS in tomato (*Solanum lycopersicum*). Likewise, Bang et al. [49] used CNN models to
149 predict TFBS in both maize (*Zea mays*) and soybean using maize DAP-seq data. Although high
150 false positive rates were observed by cross-species prediction in the latter study [49], these
151 advances demonstrate the value of DNN-based methods for TFBS prediction within and across
152 plant species.

153 In the present study, we coupled transcriptomics, *in vitro* TF-DNA interaction profiling,
154 and deep learning to construct a GRN underlying the soybean defense response to *P. sojae*
155 infection (**Fig 1**). We first inoculated hypocotyls of soybean variety Williams 82 (possesses *Rps1k*)
156 with mycelial slurries from *P. sojae* Races 1 or 25, rendering incompatible and compatible
157 interactions, respectively. Transcriptomes were generated from the hypocotyls, and differential
158 gene expression analysis was performed with expression profiles from a mock inoculation serving
159 as a baseline. Following RNA capture-based validation of the experimental design, we assessed
160 TF representation in the differentially expressed gene (DEG) set. The biological significance of
161 overrepresented TF families was inferred by clustering DEGs, assigning functional annotations to
162 each cluster, and observing TF family representation across defense-related clusters. Next, using

163 DAP-seq data for WRKY and RAV TFs differentially expressed in our DEG set, we obtained
164 promoter-localized TFBS to train DNN models for the prediction of novel WRKY and RAV
165 targets. Furthermore, cross-species target prediction was performed for MYB, WRKY, NAC, ERF,
166 and bHLH TF families using DNN models trained with available Arabidopsis DAP-seq data. We
167 observed the representation of predicted targets in our DEG set and used highly confident TF-
168 target predictions to reconstruct a GRN. Findings in this study provide insight into the regulatory
169 mechanisms governing defense against *P. sojae* and provide new/novel avenues for the molecular
170 breeding of soybean.
171

172 Results

173 Transcriptome analysis and virulence screening

174 To identify candidate genes involved in the defense response against *P. sojae*, seeds of
175 soybean variety Williams 82 were grown in germination paper and seedling hypocotyls inoculated
176 with a mycelial slurry from a Race 1 isolate (R1; incompatible interaction), a Race 25 isolate (R25;
177 compatible interaction), or sterile media (Mock) following the procedure of Dorrance et al. [50].
178 At 24 hrs post-infection (hpi), the hypocotyls were collected and used to generate 13 RNA-seq
179 libraries (4 Mock, 4 R1, and 5 R25) spanning two independent inoculations, RNA isolations, and
180 sequencing runs. Additional seedlings were maintained seven days post-infection (dpi) to compare
181 disease development across treatments (**Fig 2a**) [50]. Collectively, the RNA-seq samples
182 comprised over 560 million 100-bp paired-end reads with a mean mapping rate of 95% (**Table**
183 **S1**). Principal Component Analysis demonstrated that samples clustered according to treatment
184 and sequencing event. To circumvent the latter, we used ComBat-seq [51], a negative binomial
185 regression model, to correct batch effects. We then performed differential gene expression analysis
186 and removed any genes with expression that had been significantly changed (False Discovery Rate
187 < 0.05) between the two batches. Furthermore, we checked the expression of six genes that

188 displayed stable expression in soybean upon various biotic stresses [52] and a gene possessing a
189 *P. sojae*-inducible promoter (*GmaPPO12*) [53]. The defined reference genes showed no
190 significant differences among treatments in the present study, while *GmaPPO12* showed strong
191 induction due to *P. sojae* infection (**Data S1**). Cooperatively, all R1-inoculated hypocotyls
192 displayed a localized hypersensitive response, while those inoculated with R25 were demarcated
193 by expansive necrotic lesions (**Fig 2a**).

194 There were 6,042 DEGs (adjusted p-value < 0.05) between R1 and R25 treatments
195 compared to the Mock inoculation (**Data S1**). Among them, 2,387 (39.5%) overlapped between
196 R1 and R25, whereas 175 (2.9%) and 3,480 (57.6%) DEGs were present only in R1 or R25
197 treatments, respectively (**Fig 2b**). To validate and contextualize our findings, we isolated total
198 RNA from R1-, R25-, and Mock-inoculated hypocotyls (independent experiments from those used
199 for RNA-seq), generated adapter-ligated cDNA libraries, and performed RNA hybridization-based
200 enrichment followed by high-throughput sequencing (i.e., Capture-seq). The RNA hybridization
201 was performed with biotinylated RNA baits designed for seven genes that showed elevated
202 expression upon *P. sojae* infection (i.e., pathogen-induced genes) across all NILs reported in Lin
203 et al. [27] as well as both interaction types in our RNA-seq dataset. Baits were incorporated for
204 the six aforementioned reference genes as an internal standard. We recovered 100% of our capture
205 library. Further, 7/7 pathogen-induced genes showed significantly elevated expression in
206 inoculated vs Mock samples, while 5/6 reference genes showed stable expression across treatments
207 (**Fig S1a**,**b**).

208

209 **Identification of defense-related TF families**

210 Following transcriptome validation by Capture-seq, we used PlantTFDB [54] to identify
211 TF-annotated genes in our DEG set (genes differentially expressed in at least one interaction). We

212 found 447 (7.3% of DEGs) distributed across 43 TF families. Among these families, WRKY was
213 the most represented by total abundance (n = 65 encoding DEGs), followed by ERF (n = 56),
214 bHLH (n = 44), MYB (n = 37), and C2H2 (n = 31) (**Fig 2c**). The RAV TF family was most
215 represented by the percentage of genome-wide proportion (60%) (**Fig 2c**). Moreover, proportions
216 of WRKY, ERF, HSF, CAMTA, and RAV TF-encoding genes were significantly enriched in the
217 DEG set (hypergeometric p-value < 0.05).

218 To predict functions of the defined TF families in the present pathosystem, K-Means
219 clustering was used to segregate DEGs into nine co-expression clusters. In clusters 3 and 6
220 (hereafter "down-regulated clusters"), both compatible and incompatible interactions showed
221 reduced expression in comparison to Mock, with mean expression higher in the incompatible
222 interaction than in the compatible (**Fig 2d**). A reciprocal pattern was observed in clusters 1, 2, 4,
223 5, 7, 8, and 9 (hereafter "up-regulated clusters"), wherein the majority of genes were up-regulated
224 compared to the Mock, and the compatible interaction displayed the highest mean expression (**Fig**
225 **2d**). We explored these trends by assigning functional annotations to each gene cluster with GO
226 term and Kyoto Encyclopedia of Genes and Genomes (KEGG) pathway enrichment analyses
227 [55,56]. Interestingly, up-regulated clusters displayed enrichment for secondary metabolism and
228 signaling-related KEGG terms, particularly those inferring MAPK signal transduction
229 (DEGs/Total genes: 57/229), phenylpropanoid biosynthesis (48/214), flavonoid biosynthesis
230 (23/67), and plant-pathogen interaction (64/280) (**Fig 2e**; **Data S1**). The majority of genes
231 corresponding to these terms were differentially expressed in both compatible and incompatible
232 interactions compared to Mock, with the exception of plant-pathogen interaction and MAPK-
233 related pathways, where 27 and 35 genes, respectively, were differentially expressed exclusively
234 during the compatible interaction. Down-regulated clusters were enriched with GO and KEGG

235 terms related to primary metabolism (e.g., photosynthesis) (**Fig 2e**; **Data S1**), which likely
236 reflected a reallocation of cellular energy to defense [57].

237 Next, we examined TF representation in the co-expression clusters involved in the
238 signaling and secondary metabolic responses to *P. sojae* (i.e., up-regulated clusters). WRKY was
239 the most abundant TF family for four clusters (4, 7, 8, and 9), ERF for two clusters (1 and 5), and
240 C2H2 for cluster 2 (**Fig 2e**). Furthermore, four TF families were represented in more than half of
241 the up-regulated clusters, with ERF present in 7/7, WRKY in 6/7, C2H2 in 4/7, and MYB in 4/7.

242

243 Comprehensive identification of TFBS

244 Transcriptome analysis prompted the identification of TFBS (and thereby target genes) for
245 defense-related TF families. To this end, we performed DAP-seq for GmWRKY30, whose
246 corresponding gene (*Glyma.06G125600*) was differentially expressed by RNA-seq. In addition,
247 *GmWRKY30* homologs promoted resistance to hemibiotrophic and necrotrophic fungi in rice
248 (*Oryza sativa*) [58] and to *Cucumber mosaic virus* in Arabidopsis [59]. Treatments were prepared
249 for DAP-seq by inoculating soybean hypocotyls with an R1 *P. sojae* isolate (sample hereafter
250 referred to as "WRKY30_P1") or sterile media (hereafter "WRKY30_M1") (see "Materials and
251 Methods" for full details). WRKY30_P1 and WRKY30_M1 displayed 6,415 and 2,083 peak
252 regions, respectively, corresponding to various genomic features (**Fig 3**; **Data S3**; **Table S2**).
253 Motif enrichment analysis was then performed with MEME-ChIP [60] and demonstrated that
254 bound regions present in both samples were statistically enriched for the WRKY TF binding site,
255 W-box (TTTGAC/T), implicating that these regions were indeed bound by a WRKY TF. To
256 establish regulatory roles of GmWRKY30 during *P. sojae* infection, we obtained the peaks
257 annotated as promoters (defined as 1,000 bp up- and downstream of the transcription start site
258 [TSS]) and retained the regions shared by WRKY30_P1 and WRKY30_M1 (235 promoters) as

259 well as those found exclusively in WRKY30_P1 (1,110 promoters). Of these, 212 promoters
260 corresponded to genes in our DEG set. Interestingly, 174/212 were present exclusively in the
261 WRKY30_P1 sample (**Data S3**). Given that the only difference between WRKY30_P1 and
262 WRKY30_M1 samples was DNA methylation marks, this observation suggested that the soybean
263 genome undergoes differential methylation during *P. sojae* infection, perhaps as a mechanism to
264 prevent autoimmunity [16]. Moreover, 35/212 target genes were annotated as TFs, indicating
265 putative auto- and cross-regulatory activity of GmWRKY30 during the immune response. Thirteen
266 of the 35 TF-encoding DEGs belonged to the WRKY TF family, and all were present in the up-
267 regulated clusters (**Data S1**; **Data S3**). Furthermore, KEGG functional annotation revealed that
268 eight GmWRKY30 targets were part of the MAPK or plant-pathogen interaction pathways
269 described above (**Data S1**; **Data S3**). These data concomitantly suggest that GmWRKY30
270 regulates the expression of other TFs and signaling components during soybean-*P. sojae*
271 interaction.

272 RAV was the most abundant TF family by a percentage of genome-wide proportion in our
273 DEG set; therefore, we obtained DAP-seq data for a GmRAV TF from Wang et al. [61]. The
274 corresponding gene (*Glyma.10G204400*) was significantly up-regulated in both compatible and
275 incompatible interactions compared to Mock and displayed similar expression dynamics in Lin et
276 al. [27] upon *P. sojae* infection. In the present analysis, GmRAV was bound to 3,409 promoters
277 corresponding to 389 genes in our DEG set (**Data S1**; **Data S4**). Of these, 29 encoded TFs. One
278 hundred seventy-six of the 389 targets (45%) were present in either cluster 3 or 6 (down-regulated
279 clusters) (**Data S1**; **Data S4**). Cooperatively, functional enrichment demonstrated that GmRAV
280 targets included genes relevant to photosynthesis and carbon metabolism (**Data S1**; **Data S4**),
281 indicating that GmRAV may repress primary metabolic activity during pathogen infection.

282
283 ## DNN prediction of TFBS

284 While TFs in a structural family have the capacity to function distinctly *in vivo*, they often
285 share intrinsic CRE preference [62,63,64]. Therefore, we hypothesized that binding sites obtained
286 for a single TF could be used to predict binding sites for other members of the same family. To
287 test this hypothesis, we trained Convolutional Recurrent Neural Networks (CRNNs), which couple
288 CNN and bi-directional long short-term memory layer architecture [65] (**Fig 4**), using peak
289 summits of WRKY30_P1 and WRKY30_M1 samples with either 32- or 201-bp peak regions (**Fig**
290 **S2**). The CRNN with a 201-bp region outperformed the CRNN with a 32-bp peak region and
291 displayed an 89% validation accuracy, 90% test accuracy, and a false positive rate of less than 3%
292 (**Table 1**). We trained a similar model for GmRAV, which had an 89% validation accuracy, 89%
293 test accuracy, and a less than 3.5% false positive rate (**Table 1**). Moreover, for both GmWRKY30
294 and GmRAV CRNN models, the area under the receiver operating characteristic (auROC) curve
295 was beyond 0.88, and the area under the precision-recall curve (auPRC) beyond 0.81 (**Fig S3**). To
296 determine if a CRNN model trained for one TF could generalize to members of the same family
297 intraspecifically, we generated AmpDAP-seq data for GmWRKY2 (homologous to AtWRKY2
298 and encoded by *Glyma.06G320700*). For this sample, we first observed peak distribution across
299 genomic features (**Fig S4**; **Data S5**) and used MEME-ChIP to verify statistical enrichment of the
300 W-box CRE within peak regions. We then used peak regions to test if the GmWRKY30 CRNN
301 could predict GmWRKY2-bound sites. The prediction accuracy was above 82%, with a false
302 positive rate of less than 6% (**Fig 5a**). Furthermore, we explored the interspecific generalization
303 capacity of the GmWRKY30 CRNN by performing a cross-species prediction on AtWRKY30
304 (encoded by *AT5G24110*; homologous to GmWRKY30) DAP-seq data (generated by O'Malley

305 et al. [66] and reanalyzed by Song et al. [67]). For this analysis, the prediction accuracy was above
306 84% with a false positive rate of less than 7% (**Fig 5a**).
307

Table 1: Summary of GmWRKY and GmRAV CRNN models

Model	Train Acc. (%)	Val Acc. (%)	Test Acc. (%)	TPR (%)	TNR (%)	FPR (%)	FNR (%)
WRKY	90.97	89.77	90	33.67	56.21	2.71	7.41
RAV	89.09	89.2	89	44.88	45.33	3.49	6.3

308
309 Yet, it remained unclear whether these patterns would recur within/across TF families.
310 Therefore, we utilized DAP-seq data for AtWRKY30, AtMYB62, AtMYB108, AtMYB119,
311 AtNAC031, AtNAC053, and AtNAC057 [66,67] to train additional CRNNs. The AtWRKY30
312 model validation accuracy was 97%, test accuracy 97.33%, and false positive rate 0.13% (**Table**
313 **2**). The model was used subsequently to predict binding sites for 17 other AtWRKY TFs with
314 available DAP-seq data [66,67] and presented a mean prediction accuracy of 89% with a mean
315 false positive rate under 1% (**Fig 5b**; **Data S6**). The three AtMYB models had 92-98% validation
316 accuracies, 91-98% test accuracies, and 0.8-2.76 % false positive rates (**Table 2**) and were used to
317 predict binding sites for 5 AtMYB TFs [66,67], presenting a mean prediction accuracy of 64.92%
318 and a mean false positive rate of 1.53% (**Fig 5b**; **Data S6**). Similarly, the three AtNAC models
319 posed validation accuracies between 95.5-98%, test accuracies between 95-98%, and a false
320 positive rate ranging between 0.6-1.79% (**Table 2**). These models were used for predicting binding
321 sites for 15 other AtNAC TFs [66,67] with a mean prediction accuracy of 79.6% and a mean false
322 positive rate of 1.09% (**Fig 5b**; **Data S6**). These findings indicated that a model trained using the

323 TFBS of one family member could predict the TFBS of another member with reasonable accuracy.
324 Therefore, GmWRKY30 and GmRAV models were used to predict TFBS on promoters of the
325 DEGs from the transcriptome analysis (**Fig 5c**). To further reduce false positives, we scanned the
326 same promoter regions using Find Individual Motif Occurrences (FIMO) [68] with motifs obtained
327 from the JASPAR database [69] to find CREs. The results from the FIMO scan were overlapped
328 with our predicted sites to get a highly confident set of TFBS. From this, we obtained 3,298
329 GmWRKY targets with 267 corresponding to TF-encoding genes (60% of TFs in the DEG list).
330 Similarly, GmRAV-predicted targets included 1,925 genes, 121 of which encoded TFs (27% of
331 TFs in the DEG list) (**Data S1**).
332

Table 2: Summary of Arabidopsis data-based CRNN models used for generalization tests

Model	Common names	Val Acc. (%)	Test Acc. (%)	FPR (%)	TPR (%)	TNR (%)	FNR (%)
AT1G68320	AtMYB62	97.47	97	0.8	48	49.1	2.06
AT3G06490	AtMYB108	92.02	91	2.76	43.71	47.24	6.29
AT5G58850	AtMYB119	98.09	98	0.76	50.09	48.22	0.93
AT5G24110	AtWRKY30	97	97.33	0.13	47.41	49.89	2.57
AT1G76420	AtNAC031	95.52	95	1.79	47.6	47.34	3.26
AT3G17730	AtNAC057	97.33	97	0.98	48.31	49.16	1.54
AT3G10500	AtNAC053	98.15	98	0.6	48.96	48.72	1.73

333
334 ## Cross-species prediction of soybean TFBS
335 Based upon the interspecies generalization capacity of the GmWRKY30 model, we wanted
336 to further leverage the homology between Arabidopsis and soybean to build CRNNs and conduct
337 cross-species predictions for other defense-related TF families. In doing so, we built CRNNs for
338 AtERF, AtbHLH, AtC2H2, AtRAV, AtWRKY, AtMYB, and AtNAC TF families by combining
339 available DAP-seq data for each family. With the exception of the AtRAV and AtC2H2 models,

340 the training, validation, and testing accuracies were above 90%, and false positive rates less than
341 1.2% for all models (**Table 3**). Both AtRAV and AtC2H2 models had training, validation, and
342 testing accuracies of less than 86% with increased false negative rates and were thus not used for
343 subsequent analyses (**Table 3**). Next, we generated AmpDAP-seq data for GmMYB61 (encoded
344 by *Glyma.10G142200*) (**Fig S4**; **Data S5**) and used AtWRKY and AtMYB CRNNs to perform
345 cross-species predictions on GmWRKY30 DAP- and GmMYB61 AmpDAP-seq data,
346 respectively. Both predictions demonstrated modest accuracies (approximately 61%), yet less than
347 1% false positive rates (**Table 4**). We posited that, while Arabidopsis-to-soybean predictions
348 would likely miss some true TFBS, we could have confidence in those classified as bound.
349 Therefore, we used AtMYB, AtERF, AtNAC, and AtbHLH CRNNs to predict TFBS for promoter
350 regions of our DEGs (**Fig 5c**). Consistent with soybean CRNNs, all of the predicted TFBS were
351 overlapped with FIMO predictions to get a highly confident set of targets.
352

Table 3: Summary of Arabidopsis data-based CRNN models used for cross-species predictions

Model	Train Acc. (%)	Val Acc. (%)	Test Acc. (%)	TPR (%)	TNR (%)	FPR (%)	FNR (%)
WRKY	97.79	98.12	98.00	48.94	49.83	0.63	0.60
MYB	93.23	92.22	92.00	41.93	50.16	1.04	6.88
ERF	96.10	95.85	95.76	46.14	49.62	0.43	3.80
NAC	92.34	92.11	92.00	41.69	49.68	1.20	7.40
BHLH	96.80	96.00	96.22	47.45	48.77	0.76	3.03
RAV	74.57	75.00	73.00	22.26	50.74	0.89	26.11
C2H2	85.20	85.00	84.60	36.42	48.18	1.22	14.18

353

Table 4: Arabidopsis-to-soybean cross-species prediction results					
Model	**Cross Pred. Acc. (%)**	**TPR (%)**	**TNR (%)**	**FPR (%)**	**FNR (%)**
WRKY	61.16	5.81	55.35	0.52	38.32
MYB	60.81	10.92	49.89	0.90	38.29

354

355 ## GRN inference underpinning host defense

356 The combination of soybean and Arabidopsis CRNNs allowed the prediction of TFBS
357 corresponding to 5,505 genes in the DEG set (**Fig 6a**). Global and family-level GRNs were thereby
358 constructed with TFs represented by nodes and target genes by edges (**Fig 6b; Fig S5**). We then
359 examined TF-level TFBS to prioritize nodes in the global GRN. To be considered, nodes had to
360 possess statistically enriched binding motifs (q-value < 0.05) compared to a randomly shuffled
361 input sequence (determined by the Simple Enrichment Analysis algorithm of Bailey and Grant
362 [70]) and had to have corresponding genes expressed in the transcriptome analysis (**Fig 6d**). The
363 118 nodes meeting these criteria were prioritized by degree centrality, TF co-occurrence, and the
364 expression pattern of corresponding genes. Degree centrality was determined from outdegree
365 (number of edges directed to each node) and cumulative indegree (indegree = number of nodes to
366 which an edge is directed; cumulative indegree = combined indegree for all edges of a node). Both
367 measures were scale-free and displayed a power-law distribution (**Fig 6d**) as expected of GRN
368 architecture [71]. Furthermore, TF cooperativity/co-occurrence metrics are required to effectively
369 model causal GRNs [72]. We assessed putative TF co-occurrence with TF-COMB (Transcription
370 Factor Co-Occurrence using Market Basket analysis) [73] and selected cosine association score as
371 the objective similarity measure for co-occurring TF pairs (**Fig 6c**). Cumulative cosine (total
372 cosine association score across all co-occurrences) was determined for each node. Lastly, we

373 calculated the mean $|\log_2 FC|$ for node-corresponding genes across both interactions (R1 vs Mock
374 and R25 vs Mock) for further prioritization. Nodes/node-corresponding genes present in the upper
375 quartile for all four parameters were considered hubs (**Fig 6d**). A reciprocal approach prioritized
376 edges by indegree, cumulative outdegree (combined outdegree of all nodes to which an edge is
377 directed), sum cumulative cosine (combined cumulative cosine of all nodes to which an edge is
378 directed), and mean $|\log_2 FC|$ across both interactions (**Fig S6**).

379 Hub nodes corresponded to 14 genes encoding 13 TFs, all of which belonged to ERF and
380 WRKY families (**Fig 6d,e**). Thirteen of these were differentially expressed in the transcriptome
381 analysis and were present in co-expression clusters 1, 4, 5, and 8 (up-regulated clusters with
382 defense-related functional annotations). Furthermore, we assessed KEGG annotations for putative
383 hub node targets (n = 1,664), and 170 targets were annotated to one or more functions.
384 Interestingly, 67% (114/170) of the targets possessed primary metabolic terms whereas 33%
385 (56/170) possessed terms related to defense/secondary metabolism. It is therefore reasonable to
386 hypothesize that these hub nodes are core components of the defense-growth tradeoff in soybean
387 by regulating transcriptional reprogramming.

388 # Discussion

389 *P. sojae* is a yield-devastating soybean pathogen subject to rapid genetic diversification
390 and expansion within and across production environments. To unravel regulatory signatures of
391 host defense during *P. sojae* infection, we coupled multi-omic and computational analyses to
392 identify TF-target gene interactions at 24 hpi. In doing so, we conducted the first comparative
393 transcriptomic study for compatible and incompatible soybean-*P. sojae* interactions within a single
394 host genotype. Similar gene expression profiles were observed across the interaction types,
395 implicating significant overlap between PTI- and PTI + ETI-mediated defense at 24 hpi. Enkerli
396 et al. [74] revealed ultrastructural differences between compatible and incompatible soybean-*P.*

397 *sojae* interactions at 4 hpi, with programmed cell death and impedance of hyphal growth evident
398 in the incompatible interaction by 15 hpi. Thus, it is likely that maximal expression of PTI-
399 potentiating transcripts during incompatibility precludes or at least precedes the *P. sojae* transition
400 from biotrophy to necrotrophy (12-24 hpi [75,76]), and succedent activity reflects a reduction in
401 hypersensitivity required to offset fitness costs of induced resistance. This concept draws parallels
402 to other pathosystems in which compatible and incompatible interactions displayed consistent
403 trends in gene expression, with the incompatible interaction eliciting a heightened, more
404 immediate immune response [77,78,79]. A complementary explanation is that PTI/ETI
405 convergence is attributed to the *P. sojae* arsenal present during both compatible and incompatible
406 interactions, including MAMPs and a conserved suite of effectors [80]. Moreover, overlapping
407 expression profiles may correspond primarily to PTI signatures not targeted by *Avr*-encoded
408 effectors. Nevertheless, findings herein necessitate the investigation of compatible and
409 incompatible interactions in tandem to elucidate *Rps* gene-exclusive defense mechanisms.

410 Plant immune signaling is remarkably tunable yet robust, allowing the coordination of
411 defense and growth in a manner that maximizes host fitness [21,81,82]. Prior studies suggest signal
412 integration underpinning the defense-growth trade-off is imposed by TF regulatory networks that
413 modulate immune responses through transcriptional reprogramming [17]. In the present study, K-
414 means clustering of DEGs rendered nine gene co-expression clusters, seven of which were up-
415 regulated and corresponded to defense-related functional annotations (e.g., MAPK signaling and
416 secondary metabolism). Cooperatively, these clusters were enriched with statistically
417 overrepresented TF families (i.e., MYB, WRKY, NAC, ERF, and C2H2) known to regulate plant
418 secondary metabolism [22,23] and reported in prior soybean-*P. sojae* studies
419 [29,30,32,33,34,35,37,83]. Furthermore, WRKY and ERF were the most abundant TF families

420 across the seven clusters. This is consistent with findings in Arabidopsis where MAPK-WRKY
421 and MAPK-ERF complexes regulated core immune signaling through transcriptional
422 reprogramming [17,20,84]. The remaining gene co-expression clusters were down-regulated and
423 demarcated by growth and reproductive functional terms. Interestingly, DAP-seq suggested that
424 gene targets of RAV (the most represented TF family in the DEG set by a percentage of genome-
425 wide proportion) were enriched in these two clusters. This finding is consistent with prior studies
426 wherein GmRAV has been reported to play a role in photosynthesis, senescence, abiotic stress
427 tolerance, and phytohormone-mediated signaling [85,86,87] and act as a transcriptional repressor
428 to delay flowering [61]. To our knowledge, the present study is the first to propose a function for
429 GmRAV during immunity, where it acts as a repressor of primary metabolism. Thus, our
430 transcriptome analysis evidences transcriptional reprogramming governing the defense-growth
431 trade-off in soybean upon *P. sojae* infection.

432 DAP-seq data were generated/obtained for the most represented TF families by total
433 abundance and percentage of genome-wide proportion in the transcriptome analysis, and
434 promoter-localized DAP-seq peaks were used to train CRNNs (DNNs composed of convolutional
435 and recurrent layers) for the prediction of novel TFBS. We leveraged CRNNs for their capacity to
436 learn randomly composite, predictive sequence patterns [47]. Previous studies suggest that binding
437 site motifs, along with nearby sequence features and their organization in the genome, play a vital
438 role in TF binding. The convolutional filters in CRNNs can capture and train these binding site
439 motifs and nearby sequence features, while recurrent layers can learn their multidimensional
440 organization [47]. In addition, such hybrid model architecture has been used successfully to predict
441 TF-target interactions with human data [65,88,89]. Here, our CRNN models were capable of
442 predicting TFBS for the selected TF families in soybean and Arabidopsis with ~90% accuracy.

443 The exclusive use of DEG promoters for binding site prediction increased the likelihood that
444 targets were biologically valid, as the correlation between stable TF binding and TF regulation is
445 vastly inconsistent and oftentimes poor [72,90,91]. Moreover, CRNNs trained for one TF could
446 find TFBS for other members of the same family. We supported this notion in soybean by
447 generating binding site data for a second WRKY TF and using the pre-existing WRKY CRNN to
448 predict its targets. We validated our findings in another species by training additional CRNNs with
449 Arabidopsis DAP-seq data for WRKY, MYB, and NAC TFs and predicting TFBS for various
450 members of the respective families. In every instance, CRNNs were capable of generalizing with
451 acceptable accuracy, posing significant potential as an alternative to wet lab-based TFBS assays.
452 Altogether, findings herein reflect the ability to train highly accurate CRNNs for the prediction of
453 TFBS in plants.

454 The DNA sequence preference of TFs is largely conserved across phylogenetically-related
455 species, leading to the advent of deep learning-based approaches for cross-species TFBS
456 prediction [47,64,91]. However, recent attempts at mouse-to-human/human-to-mouse and maize-
457 to-soybean cross-species predictions suffered from high false positive rates [47,49]. We
458 hypothesized that we could overcome such limitations due to the evolutionary proximity of
459 soybean and Arabidopsis (two diploid, dicotyledonous species). In the present study, Arabidopsis-
460 to-soybean predictions had moderate accuracy (approximately 60%) with low false positive rates
461 (less than 1%). Interestingly, soybean-to-Arabidopsis predictions displayed a higher accuracy than
462 the Arabidopsis-to-soybean. Nitta et al. [92] investigated TFBS conservation between *Drosophila*
463 and mammals, finding that novel binding site specificities could arise via gene duplication and
464 subsequent divergence. Perhaps the lower Arabidopsis-to-soybean prediction accuracies reflect
465 the expansion of WRKY and MYB families in soybean, rendering soybean-specific CRE

466 preferences. Furthermore, the lower prediction accuracies may indicate contributions to TF
467 genomic occupancy beyond DNA sequence affinity (e.g., chromatin state; presence of cofactors),
468 which have been demonstrated to significantly influence immunity-related transcriptional
469 dynamics in plants [16]. Thus, the integration of complementary information (e.g., ATAC-seq
470 data) into existing CRNN frameworks will allow for more accurate model training in the future.

471 We predicted TFBS for WRKY, RAV, NAC, ERF, bHLH, and MYB TF families with
472 soybean- and Arabidopsis-based CRNNs, overlaid CRNN predictions with FIMO scans, and
473 constructed global and family-level GRNs. Within a GRN, some TFs act as hubs to regulate many
474 genes, while target genes are typically regulated by multiple TFs [72]. Therefore, we identified
475 hub nodes, which presumably have an inordinate effect on phenotype [93], by integrating motif
476 enrichment analysis, degree centrality, TF co-occurrence, and gene expression metrics.
477 Interestingly, all hub-corresponding genes encoded WRKY or ERF TFs, suggesting these families
478 are central components of the host immune response at 24 hpi. One could attribute this in part to
479 the use of intraspecies prediction for WRKY and RAV and cross-species prediction for the other
480 TF families, the latter of which was prone to high false negative rates that likely influenced degree
481 centrality. Yet, WRKY and ERF were the most represented TF families in defense-related DEG
482 clusters derived from the transcriptome analysis, which, when coupled with functional annotations
483 of hub node targets, reinforced the pertinence of the two families for host defense. Moreover, the
484 majority of hub genes identified here demonstrated differential expression in soybean upon various
485 biotic and abiotic stresses (**Fig 6d**) [27, 94,95,96,97,98,99,100,101,102] . Additional efforts must
486 be used to functionally validate TF-target predictions, which remains a bottleneck in GRN research
487 [72,103].

488 Nevertheless, this research poses limitations that must be considered. First, the inoculation
489 procedure of Dorrance et al. [50] was used in the present study: hypocotyl wounding occurred
490 prior to the placement of a mycelial slurry (sterile media for Mock tissues). It is possible that
491 mechanical tissue disruption increased damage-associated molecular pattern (DAMP)-related
492 signaling, and that DAMP + MAMP perception triggered PTI beyond what occurs *in situ* [104].
493 Second, the existing network lacks the temporal resolution required to fully elucidate dynamic
494 phenomena such as plant-pathogen interactions [72]. Thus, future experiments will include more
495 natural inoculation procedures, the integration of time-series expression and epigenomic data into
496 CRNN frameworks, the evaluation of additional defense-relevant TF families, and the molecular
497 investigation of *P. sojae* effector targets.

498 Conclusions

499 In summary, TF families emphasized in this study (particularly ERF, WRKY, and RAV)
500 are likely core components of sensory regulatory networks required for the balance of primary and
501 secondary metabolic responses to *P. sojae* infection. Interactions predicted here shed light on
502 convergent and discrete transcriptional complexes during host immunity and provide a framework
503 for data integration, functional validation, and the prediction of novel regulatory components for
504 disease resistance [21]. We also provide a framework for improved TFBS prediction by coupling
505 high-throughput sequencing data and CRNNs. Consequently, the information herein may prove
506 useful for the circumvention of *P. sojae* pathogenicity through the modulation of defense-related
507 pathways and the resultant derivation of disease-resistant soybean genotypes.

508 Materials and Methods

509 <u>Biological materials, pathogenicity testing, and RNA isolation</u>

510 For all experiments, soybean and *P. sojae* materials were generated at Iowa State University in the
511 lab of Dr. Alison Robertson. Axenic-grown *P. sojae* isolates were transferred from a 20% clarified
512 vegetable juice (V8) medium onto a soft-diluted V8 medium and incubated at 25°C in the dark as
513 defined by Dorrance et al. [50]. Concomitantly, seeds of soybean varieties Williams 82 (*Rps1k*)
514 and Williams (*Rps*) were grown on moistened germination paper at 25°C, 16 h d^{-1} light, and 90%
515 relative humidity. On day 7 of plant growth, seedling hypocotyls were incised 1 cm below the
516 cotyledonary node with a sterile razor blade and inoculated with 0.1 mL mycelial slurry of a *P.*
517 *sojae* Race 1 isolate (avirulent on *Rps1k*), a Race 25 isolate (virulent on *Rps1k*), or sterile media.
518 At 24 hpi, the mycelial slurries were washed off with deionized water, and a 2 cm fragment of
519 each hypocotyl was cut and immediately frozen in liquid nitrogen.
520
521 For each inoculation, 10 or more seedlings per treatment were kept 7 d to monitor disease
522 development. Seedlings were scored as asymptomatic or symptomatic depending on the
523 absence/presence of lesions and necrotic tissue in at least 90% of replicates. For an inoculation to
524 be successful, Williams seedlings displayed disease symptoms when infected with either *P. sojae*
525 pathotype. Williams 82 seedlings displayed hypersensitivity upon inoculation with Race 1 and
526 were symptomatic upon infection with Race 25. Moreover, mock inoculations rendered
527 asymptomatic, clean wounds for both varieties.
528
529 Total RNA was isolated from frozen Williams 82 hypocotyls with the NEB Monarch Total RNA
530 Miniprep Kit (Cat #T2010S) and quantified using a Qubit fluorometer paired with the RNA high-
531 sensitivity assay kit (Cat #Q32852). RNA purity was estimated from A260/A280 and A260/A230
532 ratios using a NanoDrop ND-1000 spectrophotometer (Thermo Fisher Scientific) and further

533 assessed by gel electrophoresis (1% agarose gel at 120V for 40 min). Samples were stored at −80
534 °C until use.

535 RNA-seq

536 Total RNA was sent to Novogene Corporation (Sacramento, CA, USA) for library preparation and
537 sequencing. RNA purity was assessed using a NanoPhotometer® spectrophotometer (Implen,
538 Westlake Village, CA, USA). RNA integrity and quantitation were monitored with the RNA Nano
539 6000 Assay Kit (Cat #5067-1511) of the Agilent Bioanalyzer 2100 system (Agilent Technologies,
540 CA, USA). Following quality control, cDNA libraries were prepared from 1 µg total RNA using
541 the NEBNext Ultra™ II RNA Library Prep Kit for Illumina (Cat #E7770S) paired with the
542 NEBNext Poly(A) mRNA Magnetic Isolation Module (Cat #E7490) following manufacturer's
543 instructions. Library quality was assessed on the Agilent Bioanalyzer 2100 system, and libraries
544 were sequenced on an Illumina platform.

545

546 Resultant short reads were processed using fastp software (v0.20.1) [105] for the removal of
547 adapter sequences and low-quality reads (Phred <33). Clean reads were then mapped to the
548 soybean reference genome (Gmax_508_v4.0.softmasked) with HISAT2 (v2.0.5) [106].
549 FeatureCounts (v1.5.0-p3) [107] was used to summarize read counts per gene. Only the genes that
550 had a mean count > 20 across all samples were considered for further analyses to improve the
551 sensitivity for differential gene expression analysis. The batch-level bias was removed using
552 Combat-Seq in the Bioconductor R package sva (v3.44.0) [51], and differential gene expression
553 analysis was performed using the DESeq2 package (v1.34.0) [108]. Genes with expression
554 significantly changed in the R1 and R25 treatments compared to the Mock treatment (adjusted *p*-
555 value ≤0.05) were deemed DEGs. Furthermore, we used two experimental batches as a factor for

556 the DESeq2 model, and any genes with an adjusted p-value ≤0.05 between the two batches were
557 removed from further analyses.
558
559 The 6,042 genes in our DEG set were clustered using the Bioconductor R package coseq (v1.17.2)
560 [109,110]. The batch effect-corrected count data were used as the input for the coseqR and centered
561 log-ratio-transformation and trimmed means of M values normalization were performed to
562 normalize the counts. Genes assigned to each cluster were used for visualization and GO and
563 KEGG enrichment analyses. For GO enrichment analysis, GO terms were downloaded from the
564 Gene Ontology Meta Annotator for Plants (GOMAP) database [111], and the enrichment analysis
565 was performed for each co-expression cluster using the TopGO Bioconductor package (v2.48.0)
566 [112]. GO terms with a *p*-value ≤0.05 were considered enriched terms. Similarly, for the KEGG
567 enrichment analysis, terms were downloaded from the KEGG database, and enrichment analysis
568 was performed using the clusterProfiler Bioconductor package (v4.4.4) [113]. KEGG pathways
569 with an adjusted *p*-value ≤0.05 were considered overrepresented. Genes encoding putative TFs
570 were annotated using PlantTFDB [54]. To calculate the statistical significance between observed
571 TF abundance in our DEG set and their genome-wide proportions, we conducted a proportion test
572 using the prop.test function in RStudio (v3.6.3) [114]. Data visualization was performed using
573 ggplot2 (v3.3.6) [115].
574
575 Capture-seq
576 Capture-seq was used to validate the expression of pathogen-induced genes and internal standards
577 (*n* = 13 genes). Hypocotyl inoculation and RNA isolation were performed as described above.
578 Adapter-ligated cDNA libraries were then prepared from total RNA using the NEBNext Ultra™
579 II RNA Library Prep Kit for Illumina (Cat #E7770S) following appendix modifications for size

580 selection of 300 nt inserts (420 nt final library size). In doing so, mRNA was fragmented using
581 First-Strand Synthesis Reaction Buffer and Random Primer Mix (2X) at 94°C for 10 min
582 (compared to 15 min in the protocol). Moreover, the incubation time during first-strand cDNA
583 synthesis was increased from 15 to 50 min at 42°C. Size selection of libraries was performed using
584 25 and then 10 µl of Agencourt AMPure XP beads (Beckman Coulter, Brea, CA, USA, Cat
585 #A63880). All libraries were quantified with a Qubit fluorometer using the dsDNA high-sensitivity
586 assay kit (Cat #Q32851) and visualized by gel electrophoresis (2% agarose gel at 100V for 60
587 min).
588
589 120-nt biotinylated RNA baits were designed by Integrated DNA Technologies (IDT, Coralville,
590 IA, USA) and encoded the sense strand of the genes of interest. Sequence capture was then
591 performed as described in the xGen hybridization protocol from IDT
592 (http://sfvideo.blob.core.windows.net/sitefinity/docs/default-source/protocol/xgen-hybridization-
593 capture-of-dna-libraries.pdf?sfvrsn=ab880a07_6) with modifications. 500 ng of each barcoded
594 Illumina library was pooled into a single 1.5 mL low-bind microcentrifuge tube and combined
595 with 5 µg of salmon sperm DNA (Cat #15632011) and 2 µl of xGen Universal BlockersTS Mix
596 (Cat #1075474) to prevent bait hybridization with repetitive elements/adapter sequences. Samples
597 were dried for ~90 min in an ISS110 SpeedVac System (Thermo Fisher Scientific). Pelleted
598 material was resuspended in 8.5 µl of 2X hybridization buffer, 2.7 µl of Hybridization Buffer
599 Enhancer, 4 µl of a working bait stock (100 attomoles/bait/µl), and 1.8 µl of nuclease-free water
600 to a final volume of 17 µl. A hybridization reaction was then performed with an initial denaturation
601 at 95°C for 30 s followed by a 16-hr incubation at 65°C. M-270 Streptavidin beads were
602 equilibrated, pelleted by a magnet, and mixed with the hybridization product for another 45-min
603 incubation at 65°C. Heated and room temperature washes were performed as recommended and

604 20 µl of nuclease-free water was added to the beads. Post-capture PCR was then performed by
605 adding the following components to the capture product: 1.25 µl of xGen library amplification
606 primer, 10 µl of 5X Phusion HF Buffer, 1 µl of 10 mM dNTP, 0.5 µl Phusion High-Fidelity DNA
607 Polymerase (Cat #M0530S), and 17.25 µl of nuclease-free water to a final volume of 50 µl.
608 Amplification settings included polymerase activation at 98°C for 45 s followed by 10 cycles of
609 denaturation at 98°C for 15 s, annealing at 60°C for 30 s, extension at 72°C for 30 s for each cycle,
610 and a final extension at 72°C for 1 min. PCR fragments were purified using Agencourt AMPure
611 XP beads (Cat #A63880) and eluted using 0.1X Tris-Ethylenediamine Tetraacetic Acid. Captured
612 libraries were quantified with a Qubit fluorometer using the dsDNA high-sensitivity assay kit (Cat
613 #Q32851). Library quality was assessed on the Agilent Bioanalyzer 2100 system (Agilent
614 Technologies, Santa Clara, CA, USA) at Novogene Corporation. Samples were then sequenced on
615 an Illumina platform with 150-bp paired-end reads.

616

617 The resultant short reads were preprocessed to remove poor-quality reads/sequencing artifacts
618 using Cutadapt (3.0) [116] and BBDuk (https://sourceforge.net/projects/bbmap/) (Phred <30). The
619 preprocessed short reads were aligned to soybean primary transcripts
620 (Gmax_275_Wm82.a2.v1.transcript_primaryTranscriptOnly.fa) obtained from Phytozome [117]
621 using Kallisto pseudoaligner (v0.46.1) [118] with default parameters. Differential gene expression
622 analysis and further data processing were performed in RStudio (v3.6.3) [114] as described for the
623 RNA-seq analysis.

624

625 DAP- and AmpDAP-seq

626 DAP- and AmpDAP-seq experiments were conducted as described previously [42]. The open
627 reading frame of each TF was cloned independently into a Gateway-compatible pIX-HALO
628 expression vector containing an N-terminal HaloTag (Arabidopsis Biological Resource Center,

629 stock #CD3-1742). Protein complexes were then expressed *in vitro* using the TNT SP6 Coupled
630 Wheat Germ Extract System (Promega, Madison, WI, USA, Cat #L4130) and purified using
631 Magne HaloTag Beads (Cat #G7282). To prepare DAP-seq samples, hypocotyls were inoculated
632 with a mycelial slurry from a *P. sojae* Race 1 isolate or sterile media as described above. Tissues
633 were collected at 24 hpi, and genomic DNA was isolated using the Zymo Research *Quick*-DNA
634 Plant/Seed Miniprep kit (Cat #D6020, Irvine, CA, USA) with the addition of 2-mercaptoethanol.
635 Three replicates per treatment were pooled to minimize biological variation, and ~5 µg DNA per
636 pool was fragmented and ligated with modified Illumina adapters. Adapter-ligated fragments were
637 then incubated with an immobilized HALO-tagged TF protein. For AmpDAP-seq, fragments were
638 PCR-amplified prior to incubation with a TF complex, permitting binding in the absence of
639 secondary modifications. In both instances, bound DNA was eluted and indexed using unique
640 barcoded primers during PCR enrichment. Indexed libraries were quantified with a Qubit
641 fluorometer paired with a dsDNA high-sensitivity assay kit (Cat #Q32851). Following
642 quantification, libraries were sequenced on an Illumina platform with 150-bp paired-end reads at
643 the University of Arkansas for Medical Sciences (Little Rock, AR, USA).
644
645 Short reads were aligned to the soybean reference genome Williams 82 Assembly 4 Annotation 1
646 (Gmax_508_v4.0.softmasked) using Burrows-Wheeler Alignment tool (v0.7.17-r1188) [119] and
647 duplicated reads were removed using sambamba (v0.6.8) [120]. DAP-seq peaks were called using
648 the Model-based Analysis of ChIP-Seq peak caller (v2.2.7.1) [121] with empty vector samples as
649 the background control. Bioconductor packages ChIPQC (v1.8.2) [122] and ChIPseeker (v1.32.0)
650 [123] were used to assess the DAP-seq data quality and peak annotation, respectively. The peak
651 annotation was performed using Williams 82 Assembly 4 Annotation 1
652 (Gmax_508_v4.0.softmasked) genome annotation.

653
654 Data preprocessing for CRNNs
655 To predict TFBS, CRNNs were trained with the aforementioned GmWRKY DAP-seq data. We
656 combined the peak regions from both samples using pandas (v1.4.0) [124] and pybedtools (v0.9.0)
657 [125] to obtain a non-redundant set of peak regions. Similarly, we obtained DAP-seq data for
658 GmRAV from Wang et al. [61] and performed peak calling as mentioned above. The two
659 biological replicates from the latter study were pooled together to get a non-redundant list of peaks.
660 Sequences corresponding to 201-bp peak summit regions were obtained using the soybean
661 reference genome with soft masked (Gmax_508_v4.0.softmasked obtained from Phytozome) and
662 the same genome assembly version used for all other processing and annotations. A negative data
663 set was created from the shuffle tool from BEDTools (v2.30.0) [126], excluding positive binding
664 site regions equal to an exact number of positive binding sites with an identical bp length. The
665 masked regions and low-intensity sequences were removed from the FASTA files. **Fig S2**
666 illustrates the selection of 201-bp bound and unbound sites. The bound sites were given the label
667 "1" (Positive), and unbound sites were labeled "0" (Negative). Both positive and negative data sets
668 were combined to obtain the complete data set for each TF. Next, the sequences were converted
669 into one-hot encoded binary information. In the one-hot encoding process, we consider the DNA
670 sequence as a one-dimensional sequence represented by 4 binary channels. The encoding was
671 conducted as follows: A = (1 0 0 0), C = (0 1 0 0), G = (0 0 10), and T= (0 0 0 1). The input for
672 each TF was (*n*, 201, 4) three-dimensional array where *n* is the number of sequences for each data
673 set.
674
675 For Arabidopsis, Song et al. [67] reanalyzed the DAP-seq data from O'Malley et al. [66], and we
676 obtained the 32-bp peak summit regions from the reanalyzed dataset. Based on Akagi et al. [48],
677 32-bp summit peak regions perform the best for Arabidopsis DNN models. Therefore, similar to

soybean, 32-bp sequences corresponding to positive and negative sets were obtained from the Arabidopsis genome sequences (genome version: TAIR 10; downloaded from The Arabidopsis Information Resource; TAIR) [127].

Model architecture, training, and testing

We used CRNN architecture for both soybean and Arabidopsis models. The input to the CRNN network was the one-hot encoded 201-bp window of DNA sequence, which was passed through a convolutional layer with 256 20-bp filters with a Rectified Linear Unit (ReLU) activation. The next layer was a convolutional layer with 64 8-bp filters with ReLU activation. This was followed by a 128-node time-distributed layer with ReLU activation. Next was a bi-directional long short-term memory network with 64 internal nodes, followed by a 50% Dropout layer. The final layer was a single sigmoid-activated neuron. See **Fig 4** for full architecture.

For the model training, data sets were split into 70% training, 15% validation, and 15% testing. The training was conducted with Keras v2.8 [128] with backend TensorFlow (v2.8) [129] using the Adam optimizer with a 0.001 learning rate. The training ran for 100 epochs. Early stopping with a patience of 20 was used to prevent overfitting. The models were trained with a batch size of 256.

Testing the capacity of models to generalize across TF families

We wanted to test the ability of a model trained using binding site data for one TF to predict binding sites across the TF family. First, we obtained AmpDAP-seq data for GmWRKY2 and obtained 201-bp peak summit regions and their corresponding DNA sequences as described above. Next, we used these as input for the model trained using GmWRKY30. Model accuracy was calculated based on the number of correct predictions/number of bound sites X 100.

704 Given the limited amount of soybean binding site data, we used Arabidopsis DAP-seq data to
705 further verify model generalization capacity. We trained models using Arabidopsis DAP-seq data
706 for AtWRKY30 (*AT5G24110*), AtMYB62 (*AT1G68320*), AtMYB108 (*AT5G58850*), AtMYB119
707 (*AT3G06490*), AtNAC031 (*AT1G76420*), AtNAC053 (*AT3G10500*), and AtNAC057
708 (*AT3G17730*) [66,67] using the methods described above. Similar to soybean, 201-bp peak summit
709 regions for 17 WRKY family members, 15 NAC family members, and five MYB family members
710 were used as input for each model. Model predictions were recorded for each family member and
711 model accuracy was calculated as described above.
712
713 Cross-species predictions using the Arabidopsis DAP-seq data
714 We built models for AtWRKY, AtMYB, AtERF, AtNAC, AtBHLH, and AtC2H2 TF families
715 using Arabidopsis DAP-seq peaks. Akagai et al. [48] used 32-bp peak summit regions to train
716 models with combined DAP-seq data to conduct cross-species prediction. Therefore, we adopted
717 a similar approach and created a combined data set for each TF family to train models using 32-
718 bp peak summit regions (with the exception of AtRAV, for which we obtained data from the
719 ReMap database [130]). In total, we combined DAP-seq data from 24 WRKY, 19 MYB, 17 NAC,
720 13 ERF, 4 C2H2, and 3 bHLH to create family-level datasets. Further, we trained models using
721 201- and 32-bp peak regions. Both model types showed high accuracies and low false positive
722 rates. However, since Akagai et al. [48] used 32-bp peak summit regions to train models to conduct
723 cross-species predictions with success, we opted for this window size for our cross-species
724 prediction. Nevertheless, our model architecture remained the same as the 201-bp models that were
725 used for soybean DAP-seq data, while the convolution layer filter lengths were different (in the
726 first CONV layer, filter length [Kernel] was 20 for soybean models and ten Arabidopsis models).
727

728 To test the ability of Arabidopsis models to successfully predict soybean binding targets, we used
729 AtWRKY- and AtMYB-trained models and 201-bp summit peak sequences obtained from
730 soybean DAP-seq (GmWRKY30) or AmpDAP data (GmMYB2) as the input for each model.
731 Model prediction was compared with true TFBS to get cross-species prediction accuracies.
732
733 Predicting new gene targets
734 For the target prediction, we selected 1,000 bp regions on both sides of the TSS (**Fig 4**), as it has
735 been shown that binding sites can reside on either side of the TSS [67]. Next, we obtained
736 predictions on *n* bp (201- or 32-bp) sliding windows throughout the 2-kb sequence. Then, based
737 on widow predictions, we determined if the gene is a potential target gene for a specific TF. If at
738 least one window had a positive prediction, we considered that a potential target.
739
740 When obtaining predictions on the target gene, the biggest challenge is finding the optimal stride
741 length for the sliding window. For soybean models, we tested three stride lengths: 10, 100, and
742 150 bp. To evaluate the best stride, we obtained predictions on 201-bp sliding windows throughout
743 the 2-kb sequence using each stride for genes with GmWRKY30 and GmRAV binding sites on
744 the promoter regions. We then calculated the model prediction with true bindings to get the best
745 stride (**Fig 4**). In both models, the 10-bp stride has the highest true positive counts. Therefore, we
746 selected the 10 bp as the optimal stride with a 201-bp window region. Leveraging the optimal
747 stride length, we predicted binding sites using GmWRKY30 and GmRAV models for all 6,042
748 DEGs. If at least one window had a positive prediction, we considered the gene a potential target
749 of the TF. Similarly, we used AtMYB, AtNAC, AtERF, and AtbHLH models to predict binding
750 sites for their respective families in soybean.
751

752 The window regions that were predicted to contain TF binding sites were scanned using FIMO
753 software [68] from the MEME suite (v5.0.5) [131] using the default parameters. To retrieve
754 matches, we obtained MEME core plants position frequency matrix files from the JASPAR
755 database [69], and any motif with a *q*-value (Benjamini–Hochberg corrected *p*-value) <0.01 was
756 used for the overlap analyses. We used pybedtools (v0.9.0) (with options: a_and_b =
757 a.intersect(b,wb=True)) [125] to get the overlaps between FIMO-predicted and CRNN-predicted
758 binding sites. Then, we annotated the overlapped binding sites using their Arabidopsis trans-acting
759 factor information obtained from the JASPAR database. Global and family-level GRNs were
760 visualized using Cytoscape (v3.9.1) [132].
761

762 Motif enrichment analysis
763 Sequences corresponding to TFBS were used as input for Simple Enrichment Analysis (v5.4.1)
764 [70] to find statistically enriched motifs with a randomly shuffled input sequence used as the
765 background. Soybean homologs for the Arabidopsis TFs were derived from the gene families of
766 the PANTHER classification system [133].
767

768 TF co-occurrence
769 Motif co-occurrence analysis was performed with Transcription Factor Co-Occurrence
770 using Market Basket analysis (TF-COMB) Python module [73] with default parameters (except
771 for the count_within() function where default options were changed to max_dist=50,
772 binarize=True, max_overlap=1).
773

774 # Accession numbers
775 Sequence data generated in this study will be submitted to the NCBI Sequence Read Archive upon
776 manuscript acceptance. In addition, any file may be obtained from the corresponding author.

Author contributions

BH, AF, and CS conducted wet lab experiments. SR, RW, and AW performed DL. BH, SR, and AW contributed to the data analysis. AR and AW designed the experiments and acquired funding. All authors contributed to the writing and editing of the manuscript and approved the final version prior to publication.

Acknowledgments

The authors acknowledge and are appreciative of the intellectual contributions of Shyaron Poudel, Jeff Gaither, and the Arkansas High-Performance Computing Center.

Supporting information

All code/additional information needed for the full reproduction of this study will be made available on GitHub upon acceptance of this manuscript. In addition, all files may be obtained from the corresponding author.

Conflicts of interest

The authors declare no conflicts of interest.

References

1. Tyler BM. Phytophthora sojae: root rot pathogen of soybean and model oomycete. Mol Plant Path. 2007;8(1):1–8. doi: 10.1111/j.1364-3703.2006.00373.x

2. Schmitthenner AF. Problems and Progress in Control of Phytophthora Root Rot of Soybean. Plant Dis. 1985; 69(4):362. doi: 10.1094/PD-69-362

3. Dorrance AE. Management of Phytophthora sojae of soybean: a review and future perspectives. Can J Plant Path. 2018;40(2):210–9. doi: 10.1080/07060661.2018.1445127

4. Sahoo DK, Abeysekara NS, Cianzio SR, Robertson AE, Bhattacharyya MK. A Novel Phytophthora sojae Resistance Rps12 Gene Mapped to a Genomic Region That Contains Several Rps Genes. PLOS ONE. 2017;12(1):e0169950. doi: 10.1371/journal.pone.0169950

807 5. Kou Y, Wang S. Broad-spectrum and durability: understanding of quantitative disease
808 resistance. Curr Opin Plant Biol. 2010;13(2):181–5. doi: 10.1016/j.pbi.2009.12.010

809 6. Sugimoto T, Kato M, Yoshida S, Matsumoto I, Kobayashi T, Kaga A, et al. Pathogenic
810 diversity of Phytophthora sojae and breeding strategies to develop Phytophthora-resistant
811 soybeans. Breed Sci. 2012;61(5):511–22. doi: 10.1270/jsbbs.61.511

812 7. Zhong C, Sun S, Yao L, Ding J, Duan C, Zhu Z. Fine Mapping and Identification of a
813 Novel Phytophthora Root Rot Resistance Locus RpsZS18 on Chromosome 2 in Soybean.
814 Front Plant Sci. 2018;9. Available from: https://doi.org/10.3389/fpls.2018.00044

815 8. Dorrance AE, Jia H, Abney TS. Evaluation of Soybean Differentials for Their Interaction
816 with Phytophthora sojae. Plant Health Prog. 2004;5(1):9. doi: 10.1094/PHP-2004-0309-
817 01-RS

818 9. Dodds PN, Rathjen JP. Plant immunity: towards an integrated view of plant–pathogen
819 interactions. Nat Rev Genet. 201;11(8):539–48. doi: 10.1038/nrg2812

820 10. Ngou BPM, Ahn HK, Ding P, Jones JDG. Mutual potentiation of plant immunity by cell-
821 surface and intracellular receptors. Nature. 2021;592(7852):110–5. doi: 10.1038/s41586-
822 021-03315-7

823 11. Jones JDG, Dangl JL. The plant immune system. Nature. 2006;444(7117):323–9. doi:
824 10.1038/nature05286

825 12. Thomma BPHJ, Nürnberger T, Joosten MHAJ. Of PAMPs and Effectors: The Blurred PTI-
826 ETI Dichotomy. Plant Cell. 2011;23(1):4–15. doi: 10.1105/tpc.110.082602

827 13. Naveed ZA, Wei X, Chen J, Mubeen H, Ali GS. The PTI to ETI Continuum in
828 Phytophthora-Plant Interactions. Front Plant Sci. 2020. Available from:
829 https://doi.org/10.3389/fpls.2020.593905

830 14. Wang Y, Tyler BM, Wang Y. Defense and Counterdefense During Plant-Pathogenic
831 Oomycete Infection. Ann Rev Microbiol. 2019;73(1):667–96. doi: 10.1146/annurev-
832 micro-020518-120022

833 15. Lu Y, Tsuda K. Intimate Association of PRR- and NLR-Mediated Signaling in Plant
834 Immunity. MPMI. 2021;34(1):3–14. doi: 10.1094/MPMI-08-20-0239-IA

835 16. Moore JW, Loake GJ, Spoel SH. Transcription Dynamics in Plant Immunity. Plant Cell.
836 2011 Aug;23(8):2809–20. doi: 10.1105/tpc.111.087346

837 17. Tsuda K, Somssich IE. Transcriptional networks in plant immunity. New Phytol.
838 2015;206(3):932–47. doi: 10.1111/nph.13286

839 18. Bai S, Liu J, Chang C, Zhang L, Maekawa T, Wang Q, et al. Structure-Function Analysis
840 of Barley NLR Immune Receptor MLA10 Reveals Its Cell Compartment Specific Activity

841 in Cell Death and Disease Resistance. PLOS Path. 2012;8(6):e1002752. doi:
842 10.1371/journal.ppat.1002752

843 19. Bhattacharjee S, Garner C, Gassmann W. New clues in the nucleus: transcriptional
844 reprogramming in effector-triggered immunity. Front Plant Sci. 2013;4. Available from:
845 https://doi.org/10.3389/fpls.2013.00364

846 20. Meng X, Zhang S. MAPK Cascades in Plant Disease Resistance Signaling. Annual Review
847 of Phytopathology. 2013;51(1):245–66. doi: 10.1146/annurev-phyto-082712-102314

848 21. Delplace F, Huard-Chauveau C, Berthomé R, Roby D. Network organization of the plant
849 immune system: from pathogen perception to robust defense induction. Plant J.
850 2022;109(2):447–70. doi: 10.1111/tpj.15462

851 22. Yang CQ, Fang X, Wu XM, Mao YB, Wang LJ, Chen XY. Transcriptional Regulation of
852 Plant Secondary Metabolism. J Integr Plant Biol. 2012;54(10):703–12. doi:
853 10.1111/j.1744-7909.2012.01161.x

854 23. Ng DWK, Abeysinghe JK, Kamali M. Regulating the Regulators: The Control of
855 Transcription Factors in Plant Defense Signaling. Int J Mol Sci. 2018;19(12):3737. doi:
856 10.3390/ijms19123737

857 24. Tyler BM, Jiang RHY, Zhou L, Tripathy S, Dou D, Torto-Alalibo T, et al. Functional
858 Genomics and Bioinformatics of the Phytophthora sojae Soybean Interaction. In:
859 Gustafson JP, Taylor J, Stacey G, editors. Genomics of Disease. New York, NY: Springer;
860 2008. p. 67–78. (Stadler Genetics Symposia Series). doi: 10.1007/978-0-387-76723-9_6

861 25. Zhou L, Mideros SX, Bao L, Hanlon R, Arredondo FD, Tripathy S, et al. Infection and
862 genotype remodel the entire soybean transcriptome. BMC Genom. 2009;10(1):49. doi:
863 10.1186/1471-2164-10-49

864 26. Wang H, Waller L, Tripathy S, St. Martin SK, Zhou L, Krampis K, et al. Analysis of Genes
865 Underlying Soybean Quantitative Trait Loci Conferring Partial Resistance to Phytophthora
866 sojae. Plant Genome. 2010;3(1). doi: 10.3835/plantgenome2009.12.0029

867 27. Lin F, Zhao M, Baumann DD, Ping J, Sun L, Liu Y, et al. Molecular response to the
868 pathogen Phytophthora sojae among ten soybean near isogenic lines revealed by
869 comparative transcriptomics. BMC Genom. 2014;15(1):18. doi: 10.1186/1471-2164-15-18

870 28. Dong L, Cheng Y, Wu J, Cheng Q, Li W, Fan S, et al. Overexpression of GmERF5, a new
871 member of the soybean EAR motif-containing ERF transcription factor, enhances
872 resistance to Phytophthora sojae in soybean. J Exp Bot. 2015;66(9):2635–47. doi:
873 10.1093/jxb/erv078

874 29. Fan S, Dong L, Han D, Zhang F, Wu J, Jiang L, et al. GmWRKY31 and GmHDL56
875 Enhances Resistance to Phytophthora sojae by Regulating Defense-Related Gene
876 Expression in Soybean. Front Plant Sci. 2017;8. Available from:
877 https://doi.org/10.3389/fpls.2017.00781

878 30. Zhao Y, Chang X, Qi D, Dong L, Wang G, Fan S, et al. A Novel Soybean ERF
879 Transcription Factor, GmERF113, Increases Resistance to Phytophthora sojae Infection in
880 Soybean. Front Plant Sci. 2017;8. Available from: https://doi.org/10.3389/fpls.2017.00299

881 31. Cheng Q, Dong L, Gao T, Liu T, Li N, Wang L, et al. The bHLH transcription factor
882 GmPIB1 facilitates resistance to Phytophthora sojae in Glycine max. J Exp Bot.
883 2018;69(10):2527–41. doi: 10.1093/jxb/ery103

884 32. Cui X, Yan Q, Gan S, Xue D, Wang H, Xing H, et al. GmWRKY40, a member of the
885 WRKY transcription factor genes identified from Glycine max L., enhanced the resistance
886 to Phytophthora sojae. BMC Plant Biol. 2019;19(1):598. doi: 10.1186/s12870-019-2132-0

887 33. Jahan MA, Harris B, Lowery M, Coburn K, Infante AM, Percifield RJ, et al. The NAC
888 family transcription factor GmNAC42–1 regulates biosynthesis of the anticancer and
889 neuroprotective glyceollins in soybean. BMC Genom. 2019;20(1):149. doi:
890 10.1186/s12864-019-5524-5

891 34. Jahan MA, Harris B, Lowery M, Infante AM, Percifield RJ, Kovinich N. Glyceollin
892 Transcription Factor GmMYB29A2 Regulates Soybean Resistance to Phytophthora sojae.
893 Plant Physiol. 2020;183(2):530–46. doi: 10.1104/pp.19.01293

894 35. Liu T, Wang H, Liu Z, Pang Z, Zhang C, Zhao M, et al. The 26S Proteasome Regulatory
895 Subunit GmPSMD Promotes Resistance to Phytophthora sojae in Soybean. Front Plant Sci.
896 2021;12. Available from: https://doi.org/10.3389/fpls.2021.513388

897 36. Yu G, Zou J, Wang J, Zhu R, Qi Z, Jiang H, et al. A soybean NAC homolog contributes to
898 resistance to Phytophthora sojae mediated by dirigent proteins. Crop J. 2022;10(2):332–
899 41. doi: 10.1016/j.cj.2021.08.009

900 37. Gao H, Jiang L, Du B, Ning B, Ding X, Zhang C, et al. GmMKK4-activated GmMPK6
901 stimulates GmERF113 to trigger resistance to Phytophthora sojae in soybean. Plant J.
902 2022;111(2):473–95. doi: 10.1111/tpj.15809

903 38. Ko DK, Brandizzi F. Network-based approaches for understanding gene regulation and
904 function in plants. Plant J. 2020;104(2):302–17. doi: 10.1111/tpj.14940

905 39. Spitz F, Furlong EEM. Transcription factors: from enhancer binding to developmental
906 control. Nat Rev Genet. 2012;13(9):613–26. doi: 10.1038/nrg3207

907 40. Krouk G, Lingeman J, Colon AM, Coruzzi G, Shasha D. Gene regulatory networks in
908 plants: learning causality from time and perturbation. Genome Biol. 2013;14(6):123. doi:
909 10.1186/gb-2013-14-6-123

910 41. Springer N, de León N, Grotewold E. Challenges of Translating Gene Regulatory
911 Information into Agronomic Improvements. Trends Plant Sci. 2019;24(12):1075–82. doi:
912 10.1016/j.tplants.2019.07.004

913 42. Bartlett A, O'Malley RC, Huang S shan C, Galli M, Nery JR, Gallavotti A, et al. Mapping
914 genome-wide transcription-factor binding sites using DAP-seq. Nat Protoc.
915 2017;12(8):1659–72. doi: 10.1038/nprot.2017.055

916 43. Windram O, Penfold CA, Denby KJ. Network Modeling to Understand Plant Immunity.
917 Ann Rev Phytopath. 2014;52(1):93–111. doi: 10.1146/annurev-phyto-102313-050103

918 44. Stormo GD, Schneider TD, Gold L, Ehrenfeucht A. Use of the 'Perceptron' algorithm to
919 distinguish translational initiation sites in E. coli. Nucleic Acids Res. 1982;10(9):2997–
920 3011. doi: 10.1093/nar/10.9.2997

921 45. Alipanahi B, Delong A, Weirauch MT, Frey BJ. Predicting the sequence specificities of
922 DNA- and RNA-binding proteins by deep learning. Nat Biotechnol. 2015;33(8):831–8.
923 doi: 10.1038/nbt.3300

924 46. Chen C, Hou J, Shi X, Yang H, Birchler JA, Cheng J. DeepGRN: prediction of transcription
925 factor binding site across cell-types using attention-based deep neural networks. BMC
926 Bioinformatics. 2021;22(1):38. doi: 10.1186/s12859-020-03952-1

927 47. Cochran K, Srivastava D, Shrikumar A, Balsubramani A, Hardison RC, Kundaje A, et al.
928 Domain-adaptive neural networks improve cross-species prediction of transcription factor
929 binding. Genome Res. 2022;32(3):512–23. doi: 10.1101/gr.275394.121

930 48. Akagi T, Masuda K, Kuwada E, Takeshita K, Kawakatsu T, Ariizumi T, et al. Genome-
931 wide cis-decoding for expression design in tomato using cistrome data and explainable
932 deep learning. Plant Cell. 2022;34(6):2174–87. doi: 10.1093/plcell/koac079

933 49. Bang S, Galli M, Crisp PA, Gallavotti A, Schmitz RJ. Identifying transcription factor-DNA
934 interactions using machine learning. in silico Plants. 2022;diac014. doi:
935 10.1093/insilicoplants/diac014

936 50. Dorrance AE, Berry SA, Anderson TR, Meharg C. Isolation, Storage, Pathotype
937 Characterization, and Evaluation of Resistance for Phytophthora sojae in Soybean. Plant
938 Health Prog. 2008;9(1):35. doi: 10.1094/PHP-2008-0118-01-DG

939 51. Zhang Y, Parmigiani G, Johnson WE. ComBat-seq: batch effect adjustment for RNA-seq
940 count data. NAR Genom Bioinform. 2020;2(3):lqaa078. doi: 10.1093/nargab/lqaa078

941 52. Bansal R, Mittapelly P, Cassone BJ, Mamidala P, Redinbaugh MG, Michel A.
942 Recommended Reference Genes for Quantitative PCR Analysis in Soybean Have Variable
943 Stabilities during Diverse Biotic Stresses. PLOS ONE. 2015;10(8):e0134890. doi:
944 10.1371/journal.pone.0134890

945 53. Chai C, Lin Y, Shen D, Wu Y, Li H, Dou D. Identification and Functional Characterization
946 of the Soybean GmaPPO12 Promoter Conferring Phytophthora sojae Induced Expression.
947 PLOS ONE. 2013;8(6):e67670. doi: 10.1371/journal.pone.0067670

948 54. Tian F, Yang DC, Meng YQ, Jin J, Gao G. PlantRegMap: charting functional regulatory
949 maps in plants. Nucleic Acids Res. 2020;48(D1):D1104–13. doi: 10.1093/nar/gkz1020

950 55. Ashburner M, Ball CA, Blake JA, Botstein D, Butler H, Cherry JM, et al. Gene Ontology:
951 tool for the unification of biology. Nat Genet. 2000;25(1):25–9. doi: 10.1038/75556

952 56. Kanehisa M, Goto S. KEGG: Kyoto Encyclopedia of Genes and Genomes. Nucleic Acids
953 Res. 2000;28(1):27–30. doi: 10.1093/nar/28.1.27

954 57. Rojas C, Senthil-Kumar M, Tzin V, Mysore K. Regulation of primary plant metabolism
955 during plant-pathogen interactions and its contribution to plant defense. Front Plant Sci.
956 2014;5. Available from: https://doi.org/10.3389/fpls.2014.00017

957 58. Peng X, Hu Y, Tang X, Zhou P, Deng X, Wang H, et al. Constitutive expression of rice
958 WRKY30 gene increases the endogenous jasmonic acid accumulation, PR gene expression
959 and resistance to fungal pathogens in rice. Planta. 2012;236(5):1485–98. doi:
960 10.1007/s00425-012-1698-7

961 59. Zou L, Yang F, Ma Y, Wu Q, Yi K, Zhang D. Transcription factor WRKY30 mediates
962 resistance to Cucumber mosaic virus in Arabidopsis. Biochem Biophys Res Comm.
963 2019;517(1):118–24. doi: 10.1016/j.bbrc.2019.07.030

964 60. Machanick P, Bailey TL. MEME-ChIP: motif analysis of large DNA datasets.
965 Bioinformatics. 2011;27(12):1696–7. doi: 10.1093/bioinformatics/btr189

966 61. Wang Y, Xu C, Sun J, Dong L, Li M, Liu Y, et al. GmRAV confers ecological adaptation
967 through photoperiod control of flowering time and maturity in soybean. Plant Physiol.
968 2021;187(1):361–77. doi: 10.1093/plphys/kiab255

969 62. Jolma A, Yan J, Whitington T, Toivonen J, Nitta KR, Rastas P, et al. DNA-Binding
970 Specificities of Human Transcription Factors. Cell. 2013;152(1):327–39. doi:
971 10.1016/j.cell.2012.12.009

972 63. Kribelbauer JF, Rastogi C, Bussemaker HJ, Mann RS. Low-Affinity Binding Sites and the
973 Transcription Factor Specificity Paradox in Eukaryotes. Annu Rev Cell Dev Biol.
974 2019;35:357–79. doi: 10.1146/annurev-cellbio-100617-062719

975 64. Kelley DR. Cross-species regulatory sequence activity prediction. PLOS Comp Biol.
976 2020;16(7):e1008050. doi: 10.1371/journal.pcbi.1008050

977 65. Quang D, Xie X. DanQ: a hybrid convolutional and recurrent deep neural network for
978 quantifying the function of DNA sequences. Nucleic Acids Res. 2016;44(11):e107. doi:
979 10.1093/nar/gkw226

980 66. O'Malley RC, Huang S shan C, Song L, Lewsey MG, Bartlett A, Nery JR, et al. Cistrome
981 and Epicistrome Features Shape the Regulatory DNA Landscape. Cell. 2016;165(5):1280–
982 92. doi: 10.1016/j.cell.2016.04.038

983 67. Song Q, Lee J, Akter S, Rogers M, Grene R, Li S. Prediction of condition-specific
984 regulatory genes using machine learning. Nucleic Acids Res. 2020;48(11):e62. doi:
985 10.1093/nar/gkaa264

986 68. Grant CE, Bailey TL, Noble WS. FIMO: scanning for occurrences of a given motif.
987 Bioinformatics. 2011;27(7):1017–8. doi: 10.1093/bioinformatics/btr064

988 69. Castro-Mondragon JA, Riudavets-Puig R, Rauluseviciute I, Berhanu Lemma R, Turchi L,
989 Blanc-Mathieu R, et al. JASPAR 2022: the 9th release of the open-access database of
990 transcription factor binding profiles. Nucleic Acids Res. 2022;50(D1):D165–73. doi:
991 10.1093/nar/gkab1113

992 70. Bailey TL, Grant CE. SEA: Simple Enrichment Analysis of motifs. bioRxiv. 2021. doi:
993 10.1101/2021.08.23.457422

994 71. Albert R. Scale-free networks in cell biology. J Cell Sci. 2005;118(21):4947–57. doi:
995 10.1242/jcs.02714

996 72. Alvarez JM, Brooks MD, Swift J, Coruzzi GM. Time-Based Systems Biology Approaches
997 to Capture and Model Dynamic Gene Regulatory Networks. Ann Rev Plant Biol.
998 2021;72(1):105–31. doi: 10.1146/annurev-arplant-081320-090914

999 73. Bentsen M, Heger V, Schultheis H, Kuenne C, Looso M. TF-COMB–Discovering
1000 grammar of transcription factor binding sites. Comp Struct Biotech J. 2022;20:4040-51.
1001 doi: 10.1016/j.csbj.2022.07.025

1002 74. Enkerli K, Mims CW, Hahn MG. Ultrastructure of compatible and incompatible
1003 interactions of soybean roots infected with the plant pathogenic oomycete Phytophthora
1004 sojae. Can J Bot. 1997;75(9):1493–508. doi: 10.1139/b97-864

1005 75. Ward EWB. The interaction of soya beans with Phytophthora megasperma f.sp. glycinea:
1006 pathogenicity. Biological control of soil-borne plant pathogens. 1990;311–27.

1007 76. Moy P, Qutob D, Chapman BP, Atkinson I, Gijzen M. Patterns of Gene Expression Upon
1008 Infection of Soybean Plants by Phytophthora sojae. MPMI. 2004;17(10):1051–62. doi:
1009 10.1094/MPMI.2004.17.10.1051

1010 77. Rinaldi C, Kohler A, Frey P, Duchaussoy F, Ningre N, Couloux A, et al. Transcript
1011 Profiling of Poplar Leaves upon Infection with Compatible and Incompatible Strains of the
1012 Foliar Rust Melampsora larici-populina. Plant Physiol. 2007;144(1):347–66. doi:
1013 10.1104/pp.106.094987

1014 78. Mine A, Seyfferth C, Kracher B, Berens ML, Becker D, Tsuda K. The Defense
1015 Phytohormone Signaling Network Enables Rapid, High-Amplitude Transcriptional
1016 Reprogramming during Effector-Triggered Immunity. Plant Cell. 2018;30(6):1199–219.
1017 doi: 10.1105/tpc.17.00970

1018 79. Duan Y, Duan S, Armstrong MR, Xu J, Zheng J, Hu J, et al. Comparative Transcriptome
1019 Profiling Reveals Compatible and Incompatible Patterns of Potato Toward Phytophthora
1020 infestans. G3-Genes Genom Genet. 2020;10(2):623–34. doi: 10.1534/g3.119.400818

1021 80. Yuan M, Ngou BPM, Ding P, Xin XF. PTI-ETI crosstalk: an integrative view of plant
1022 immunity. Curr Opin Plant Biol. 2021;62:102030. doi: 10.1016/j.pbi.2021.102030

1023 81. Denancé N, Sánchez-Vallet A, Goffner D, Molina A. Disease resistance or growth: the role
1024 of plant hormones in balancing immune responses and fitness costs. Front Plant Sci.
1025 2013;4. Available from: https://doi.org/10.3389/fpls.2013.00155

1026 82. Kim Y, Tsuda K, Igarashi D, Hillmer RA, Sakakibara H, Myers CL, et al. Mechanisms
1027 Underlying Robustness and Tunability in a Plant Immune Signaling Network. Cell Host
1028 Microbe. 2014;15(1):84–94. doi: 10.1016/j.chom.2013.12.002

1029 83. Zhang C, Cheng Q, Wang H, Gao H, Fang X, Chen X, et al. GmBTB/POZ promotes the
1030 ubiquitination and degradation of LHP1 to regulate the response of soybean to
1031 Phytophthora sojae. Commun Biol. 2021;4(1):1–15. doi: 10.1038/s42003-021-01907-7

1032 84. Mao G, Meng X, Liu Y, Zheng Z, Chen Z, Zhang S. Phosphorylation of a WRKY
1033 Transcription Factor by Two Pathogen-Responsive MAPKs Drives Phytoalexin
1034 Biosynthesis in Arabidopsis. Plant Cell. 2011;23(4):1639–53. doi:
1035 10.1105/tpc.111.084996

1036 85. Zhao L, Luo Q, Yang C, Han Y, Li W. A RAV-like transcription factor controls
1037 photosynthesis and senescence in soybean. Planta. 2008;227(6):1389–99. doi:
1038 10.1007/s00425-008-0711-7

1039 86. Zhao L, Hao D, Chen L, Lu Q, Zhang Y, Li Y, et al. Roles for a soybean RAV-like
1040 orthologue in shoot regeneration and photoperiodicity inferred from transgenic plants. J
1041 Exp Bot. 2012;63(8):3257–70. doi: 10.1093/jxb/ers056

1042 87. Zhao SP, Xu ZS, Zheng WJ, Zhao W, Wang YX, Yu TF, et al. Genome-Wide Analysis of
1043 the RAV Family in Soybean and Functional Identification of GmRAV-03 Involvement in
1044 Salt and Drought Stresses and Exogenous ABA Treatment. Front Plant Sci. 2017;8.
1045 Available from: https://doi.org/10.3389/fpls.2017.00905

1046 88. Quang D, Xie X. FactorNet: A deep learning framework for predicting cell type specific
1047 transcription factor binding from nucleotide-resolution sequential data. Methods.
1048 2019;166:40–7. doi: 10.1016/j.ymeth.2019.03.020

1049 89. Srivastava D, Aydin B, Mazzoni EO, Mahony S. An interpretable bimodal neural network
1050 characterizes the sequence and preexisting chromatin predictors of induced transcription
1051 factor binding. Genome Biol. 2021;22(1):20. doi: 10.1186/s13059-020-02218-6
1052 90. Swift J, Coruzzi GM. A matter of time — How transient transcription factor interactions
1053 create dynamic gene regulatory networks. Biochim Biophys Acta Gene Regul Mech.
1054 2017;1860(1):75–83. doi: 10.1016/j.bbagrm.2016.08.007

1055 91. Brooks MD, Juang CL, Katari MS, Alvarez JM, Pasquino A, Shih HJ, et al. ConnecTF: A
1056 platform to integrate transcription factor–gene interactions and validate regulatory
1057 networks. Plant Physiol. 2021;185(1):49–66. doi: 10.1093/plphys/kiaa012

1058 92. Nitta KR, Jolma A, Yin Y, Morgunova E, Kivioja T, Akhtar J, et al. Conservation of
1059 transcription factor binding specificities across 600 million years of bilateria evolution.
1060 Ren B, editor. eLife. 2015;4:e04837. doi: 10.7554/eLife.04837

1061 93. Varala K, Marshall-Colón A, Cirrone J, Brooks MD, Pasquino AV, Léran S, et al.
1062 Temporal transcriptional logic of dynamic regulatory networks underlying nitrogen
1063 signaling and use in plants. Proc. Natl. Acad. Sci. U.S.A. 2018;115(25):6494–9. doi:
1064 10.1073/pnas.1721487115

1065 94. Atencio L, Salazar J, Lauter AN, Gonzales MD, O'Rourke JA, Graham MA. Characterizing
1066 short and long term iron stress responses in iron deficiency tolerant and susceptible soybean
1067 (Glycine max L. Merr.). Plant Stress. 2021;2:100012. doi: 10.1016/j.stress.2021.100012

1068 95. Liu Y, Xue Y, Xie B, Zhu S, Lu X, Liang C, Tian J. Complex gene regulation between
1069 young and old soybean leaves in responses to manganese toxicity. Plant Phys and Biochem.
1070 2020;155:231-42. doi: 10.1016/j.plaphy.2020.07.002

1071 96. Chen LM, Fang YS, Zhang CJ, Hao QN, Cao D, Yuan SL, Chen HF, Yang ZL, Chen SL,
1072 Shan ZH, Liu BH. GmSYP24, a putative syntaxin gene, confers osmotic/drought, salt stress
1073 tolerances and ABA signal pathway. Sci Rep. 2019;9(1):1-2. doi: 10.1038/s41598-019-
1074 42332-5

1075 97. Zhang H, Yang Y, Sun C, Liu X, Lv L, Hu Z, Yu D, Zhang D. Up-regulating GmETO1
1076 improves phosphorus uptake and use efficiency by promoting root growth in soybean. Plant
1077 Cell Env. 2020;43(9):2080-94. doi: 10.1111/pce.13816

1078 98. Chang C, Tian L, Ma L, Li W, Nasir F, Li X, Tran LS, Tian C. Differential responses of
1079 molecular mechanisms and physiochemical characters in wild and cultivated soybeans
1080 against invasion by the pathogenic Fusarium oxysporum Schltdl. Physiol Plant.
1081 2019;166(4):1008-25. doi: 10.1111/ppl.12870

1082 99. McCabe CE, Cianzio SR, O'Rourke JA, Graham MA. Leveraging RNA-Seq to
1083 characterize resistance to Brown stem rot and the Rbs3 locus in soybean. Mol Plant-
1084 Microbe Interact. 2018;31(10):1083-94. doi: 10.1094/MPMI-01-18-0009-R

1085 100. Liu X, Chu S, Sun C, Xu H, Zhang J, Jiao Y, Zhang D. Genome-wide identification
1086 of low phosphorus responsive microRNAs in two soybean genotypes by high-throughput
1087 sequencing. Funct Integr Genomics. 2020; 20(6):825-38. doi: 10.1007/s10142-020-00754-
1088 9

1089 101. Zhao J, Zheng L, Wei J, Wang Y, Chen J, Zhou Y, Chen M, Wang F, Ma Y, Xu
1090 ZS. The soybean PLATZ transcription factor GmPLATZ17 suppresses drought tolerance
1091 by interfering with stress-associated gene regulation of GmDREB5. Crop J. 2022. doi:
1092 10.1016/j.cj.2022.03.009

1093 102. Han X, Wang J, Zhang Y, Kong Y, Dong H, Feng X, Li T, Zhou C, Yu J, Xin D,
1094 Chen Q. Changes in the m6A RNA methylome accompany the promotion of soybean root
1095 growth by rhizobia under cadmium stress. J Haz Mat. 2023;441:129843. doi:
1096 10.1016/j.jhazmat.2022.129843

1097 103. Schrynemackers M, Kueffner R, Geurts P. On protocols and measures for the
1098 validation of supervised methods for the inference of biological networks. Front Genet.
1099 2013;4. Available from: https://doi.org/10.3389/fgene.2013.00262

1100 104. Zhou F, Emonet A, Dénervaud Tendon V, Marhavy P, Wu D, Lahaye T, et al. Co-
1101 incidence of Damage and Microbial Patterns Controls Localized Immune Responses in
1102 Roots. Cell. 2020;180(3):440-453.e18. doi: 10.1016/j.cell.2020.01.013

1103 105. Chen S, Zhou Y, Chen Y, Gu J. fastp: an ultra-fast all-in-one FASTQ preprocessor.
1104 Bioinformatics. 2018;34(17):i884–90. doi: 10.1093/bioinformatics/bty560

1105 106. Kim D, Paggi JM, Park C, Bennett C, Salzberg SL. Graph-based genome alignment
1106 and genotyping with HISAT2 and HISAT-genotype. Nat Biotechnol. 2019;37(8):907–15.
1107 doi: 10.1038/s41587-019-0201-4

1108 107. Liao Y, Smyth GK, Shi W. featureCounts: an efficient general purpose program for
1109 assigning sequence reads to genomic features. Bioinformatics. 2014;30(7):923–30. doi:
1110 10.1093/bioinformatics/btt656
1111 108. Love MI, Huber W, Anders S. Moderated estimation of fold change and dispersion
1112 for RNA-seq data with DESeq2. Genome Biol. 2014;15(12):550. doi: 10.1186/s13059-
1113 014-0550-8

1114 109. Rau A, Maugis-Rabusseau C. Transformation and model choice for RNA-seq co-
1115 expression analysis. Brief Bioinform. 2018;19(3):425–36. doi: 10.1093/bib/bbw128

1116 110. Godichon-Baggioni A, Maugis-Rabusseau C, Rau A. Clustering transformed
1117 compositional data using K-means, with applications in gene expression and bicycle
1118 sharing system data. J Appl Stat. 2019;46(1):47–65. doi: 10.1080/02664763.2018.1454894

1119 111. Wimalanathan K, Lawrence-Dill CJ. Gene Ontology Meta Annotator for Plants
1120 (GOMAP). Plant Methods. 2021;17(1):54. doi: 10.1186/s13007-021-00754-1

1121 112. Alexa A, Rahnenführer J. Gene set enrichment analysis with topGO. Bioconductor
1122 Improv. 2009;27:1-26.

1123 113. Yu G, Wang LG, Han Y, He QY. clusterProfiler: an R Package for Comparing
1124 Biological Themes Among Gene Clusters. OMICS J Integr Biol. 2012;16(5):284–7. doi:
1125 10.1089/omi.2011.0118

1126 114. RStudio T. RStudio: integrated development for R. Rstudio Team, PBC, Boston,
1127 MA URL http://www. rstudio. com. 2020.

1128 115. Wickham H, Chang W, Wickham MH. Package 'ggplot2'. Create elegant data
1129 visualizations using the grammar of graphics. Version. 2016;2(1):1-89.

1130 116. Martin M. Cutadapt removes adapter sequences from high-throughput sequencing
1131 reads. EMBnet j.2011;17(1):10–2. doi: 10.14806/ej.17.1.200

1132 117. Goodstein DM, Shu S, Howson R, Neupane R, Hayes RD, Fazo J, et al. Phytozome:
1133 a comparative platform for green plant genomics. Nucleic Acids Res.
1134 2012;40(D1):D1178–86. doi: 10.1093/nar/gkr944

1135 118. Bray NL, Pimentel H, Melsted P, Pachter L. Near-optimal probabilistic RNA-seq
1136 quantification. Nat Biotechnol. 2016;34(5):525–7. doi: 10.1038/nbt.3519

1137 119. Li H, Durbin R. Fast and accurate short read alignment with Burrows–Wheeler
1138 transform. Bioinformatics. 2009;25(14):1754–60. doi: 10.1093/bioinformatics/btp324

1139 120. Tarasov A, Vilella AJ, Cuppen E, Nijman IJ, Prins P. Sambamba: fast processing
1140 of NGS alignment formats. Bioinformatics. 2015;31(12):2032–4. doi:
1141 10.1093/bioinformatics/btv098

1142 121. Zhang Y, Liu T, Meyer CA, Eeckhoute J, Johnson DS, Bernstein BE, et al. Model-
1143 based Analysis of ChIP-Seq (MACS). Genome Biol. 2008;9(9):R137. doi: 10.1186/gb-
1144 2008-9-9-r137

1145 122. Carroll TS, Liang Z, Salama R, Stark R, de Santiago I. Impact of artifact removal
1146 on ChIP quality metrics in ChIP-seq and ChIP-exo data. Front Genet. 2014;5. Available
1147 from: https://doi.org/10.3389/fgene.2014.00075

1148 123. Yu G, Wang LG, He QY. ChIPseeker: an R/Bioconductor package for ChIP peak
1149 annotation, comparison and visualization. Bioinformatics. 2015;31(14):2382–3. doi:
1150 10.1093/bioinformatics/btv145

1151 124. McKinney W. pandas: a Foundational Python Library for Data Analysis and
1152 Statistics. 2011;9.

1153 125. Dale RK, Pedersen BS, Quinlan AR. Pybedtools: a flexible Python library for
1154 manipulating genomic datasets and annotations. Bioinformatics. 2011;27(24):3423–4. doi:
1155 10.1093/bioinformatics/btr539

1156 126. Quinlan AR. BEDTools: The Swiss-Army Tool for Genome Feature Analysis. Curr
1157 Protoc Bioinformatics. 2014;47(1):11.12.1-11.12.34. doi: 10.1002/0471250953.bi1112s47

1158 127. Berardini TZ, Reiser L, Li D, Mezheritsky Y, Muller R, Strait E, et al. The
1159 arabidopsis information resource: Making and mining the "gold standard" annotated
1160 reference plant genome. genesis. 2015;53(8):474–85. doi: 10.1002/dvg.22877

1161 128. Chollet F. keras. 2015.

129. Abadi M, Barham P, Chen J, Chen Z, Davis A, Dean J, Devin M, Ghemawat S, Irving G, Isard M, Kudlur M. {TensorFlow}: a system for {Large-Scale} machine learning. In12th USENIX symposium on operating systems design and implementation (OSDI 16) 2016 (pp. 265-283).

130. Hammal F, de Langen P, Bergon A, Lopez F, Ballester B. ReMap 2022: a database of Human, Mouse, Drosophila and Arabidopsis regulatory regions from an integrative analysis of DNA-binding sequencing experiments. Nucleic Acids Res. 2022;50(D1):D316–25. doi: 10.1093/nar/gkab996

131. Bailey TL, Johnson J, Grant CE, Noble WS. The MEME Suite. Nucleic Acids Res. 2015 Jul 1;43(W1):W39–49. doi: 10.1093/nar/gkv416

132. Shannon P, Markiel A, Ozier O, Baliga NS, Wang JT, Ramage D, et al. Cytoscape: A Software Environment for Integrated Models of Biomolecular Interaction Networks. Genome Res. 2003;13(11):2498–504. doi: 10.1101/gr.1239303

133. Mi H, Muruganujan A, Huang X, Ebert D, Mills C, Guo X, Thomas PD. Protocol Update for large-scale genome and gene function analysis with the PANTHER classification system (v. 14.0). Nat Protoc. 2019;14(3):703-21. doi: 10.1038/s41596-019-0128-8

Supporting information captions

Fig S1 Capture-seq validation of RNA-seq data. (**a**) Heatmap of reference gene expression in RNA- and Capture-seq. (**b**) Heatmap of pathogen-induced gene expression.

Fig S2 Selection of 201-bp bound (peak regions) and unbound sites (negative dataset) during model training.

Fig S3 auROC and auPRC curves for soybean data-trained models. (**a**) auROC curve for GmWRKY30 CRNN. (**b**) auROC curve for GmRAV CRNN. (**c**) auPRC curve for GmWRKY30 CRNN. (**d**) auPRC curve for GmRAV CRNN.

Fig S4 AmpDAP-seq data for GmMYB61 and GmWRKY2. (**a**) Heatmap of DAP peak binding within 1,000 bp of the TSS region. (**b**) Distribution of DAP peaks across genomic features.

Fig S5 GRNs for defense-related TF families. (**a**) bHLH GRN. (**b**) ERF GRN. (**c**) MYB GRN. (**d**) NAC GRN. (**e**) RAV GRN. (**f**) WRKY GRN.

Fig S6 Prioritization of target genes. (**a**) Density plots of indegree, cumulative outdegree, sum cumulative cosine, and mean $|\log_2 FC|$ (Mean $|FC|$) for target genes. Red polygons represent the upper quartile for each parameter. Furthermore, 254 targets were in the upper quarter for all four parameters. (**b**) Heatmap depicting the $\log_2 FC$ (FC) of prioritized target genes across both interactions.

Table S1 RNA-seq mapping statistics.

1204
1205 **Table S2** Mapping statistics for DAP- and AmpDAP-seq.
1206
1207 **Data S1** DEGs from RNA-seq, corresponding co-expression cluster assignments, functional
1208 annotations, and target gene assignments.
1209
1210 **Data S2** Capture-seq gene list and expression data.
1211
1212 **Data S3** GmWRKY30 DAP-seq binding site data.
1213
1214 **Data S4** GmRAV DAP-seq binding site data.
1215
1216 **Data S5** GmMYB61 and GmWRKY2 AmpDAP-seq binding site data.
1217
1218 **Data S6** Arabidopsis generalization prediction accuracies.
1219

1220 Figure and table captions

1221 **Fig 1 Schematic overview of the study design.** (**a**) Soybean plants harboring *Rps1k* were
1222 inoculated with a Race 1 *P. sojae* isolate, Race 25 isolate, or sterile media. Inoculated hypocotyls
1223 were used for RNA-seq. Capture-seq was performed subsequently to validate the RNA-seq data.
1224 (**b**) Overrepresented TF families were identified from the RNA-seq analysis. DAP-seq data was
1225 generated/obtained for the families most represented by total abundance and percentage of
1226 genome-wide proportion. (**c**) DL models were trained using DAP-seq binding site data. The
1227 capacity of some models to generalize across a given TF family was performed intra- and
1228 interspecifically. For several TF families of interest, soybean- or Arabidopsis-based DNNs were
1229 trained and used to predict TFBS. (**d**) DNN predictions were overlapped with FIMO motif scans,
1230 and the highly confident targets were used to construct a GRN.
1231
1232 **Fig 2 Pathogenicity testing and transcriptome analysis.** (**a**) Disease development in Race 25-
1233 (top) and Race 1-treated (bottom) hypocotyls at seven days post-infection. (**b**) Venn diagram of
1234 DEGs between different treatments. (**c**) TF representation among DEGs from RNA-seq. WRKY
1235 was the most represented TF family by total abundance and RAV by the percentage of genome-
1236 wide proportion. (**d**) K-means clustering of DEGs. DEGs were assigned to nine co-expression
1237 clusters. Of these, seven displayed increased expression ($\log_2$FC [FC] >0) in infected vs Mock
1238 treatments, while two demonstrated decreased expression (FC <0). (**e**) Functional enrichment and
1239 TF representation for gene co-expression clusters. (left panel) Top five GO categories by *p*-value.
1240 (middle panel) Top five KEGG terms by adjusted *p*-value (≤0.05). (right panel) top 3 TF families
1241 (abundance) for each cluster.
1242
1243 **Fig 3 DAP-seq identification of GmWRKY30 and GmRAV TFBS.** (**a**) Distribution of DAP-
1244 seq peaks across genomic features. (**b**) Distance of peaks from the TSS.
1245
1246 **Fig 4 Schematic illustration of CRNN architecture and TFBS prediction.**
1247
1248 **Fig 5 Generalization testing for soybean and Arabidopsis CRNNs and schematic illustration**
1249 **of TFBS prediction for defense-related TF families.** (**a**) The GmWRKY30 CRNN was used to

predict TFBS interspecifically with AtWRKY30 DAP-seq data (left barplot) and intraspecifically with GmWRKY2 AmpDAP-seq data (right barplot). (**b**) AtWRKY, AtMYB, and AtNAC CRNNs were trained with available DAP-seq data and used to predict binding sites for other members of their respective families. (**c**) The Arabidopsis-based models, along with the GmWRKY30 and GmRAV models, were used to predict TFBS in our DEG set. These predictions were overlaid with FIMO scans to elucidate TF-target gene interactions.

Fig 6 GRN inference at 24 hpi. (**a**) (left) $\log_2$FC (FC) of DEGs across interaction types, (middle) WRKY and RAV binding site representation in the DEG set derived from DAP-seq, and (right) binding site representation for each TF family in the DEG set derived from CRNN + FIMO prediction. The bar plot shows the total number of target genes for each family, as well as the number of TF-encoding target genes (light green). (**b**) Hairball of the global GRN. Nodes and edges represent TFs and target genes, respectively. Node size corresponds to outdegree. (**c**) Scatterplot of the top co-occurring TF pairs by cosine association score identified with TF-COMB. The datapoint color reflects the total number of shared targets for a given TF pair. (**d**) Prioritization of nodes. Nodes that were statistically enriched by Simple Enrichment Analysis and were represented in the transcriptome analysis (n = 118) were prioritized by outdegree, cumulative indegree, cumulative cosine, and mean |log2FC| (Mean |FC|). Blue polygons represent the upper quartile for each parameter. Fourteen genes/13 TFs were in the upper quarter for all four parameters. (**e**) Hairball of the hub nodes. Node size corresponds to outdegree.

Table 1 Summary of GmWRKY and GmRAV CRNN models. TPR: True Positive Rate; TNR: True Negative Rate; FPR: False Positive Rate; FNR: False Negative Rate

Table 2 Summary of Arabidopsis data-based CRNN models used for generalization tests. TPR: True Positive Rate; TNR: True Negative Rate; FPR: False Positive Rate; FNR: False Negative Rate

Table 3 Summary of Arabidopsis data-based CRNN models used for cross-species predictions. TPR: True Positive Rate; TNR: True Negative Rate; FPR: False Positive Rate; FNR: False Negative Rate

Table 4 Arabidopsis-to-soybean cross-species prediction results. TPR: True Positive Rate; TNR: True Negative Rate; FPR: False Positive Rate; FNR: False Negative Rate

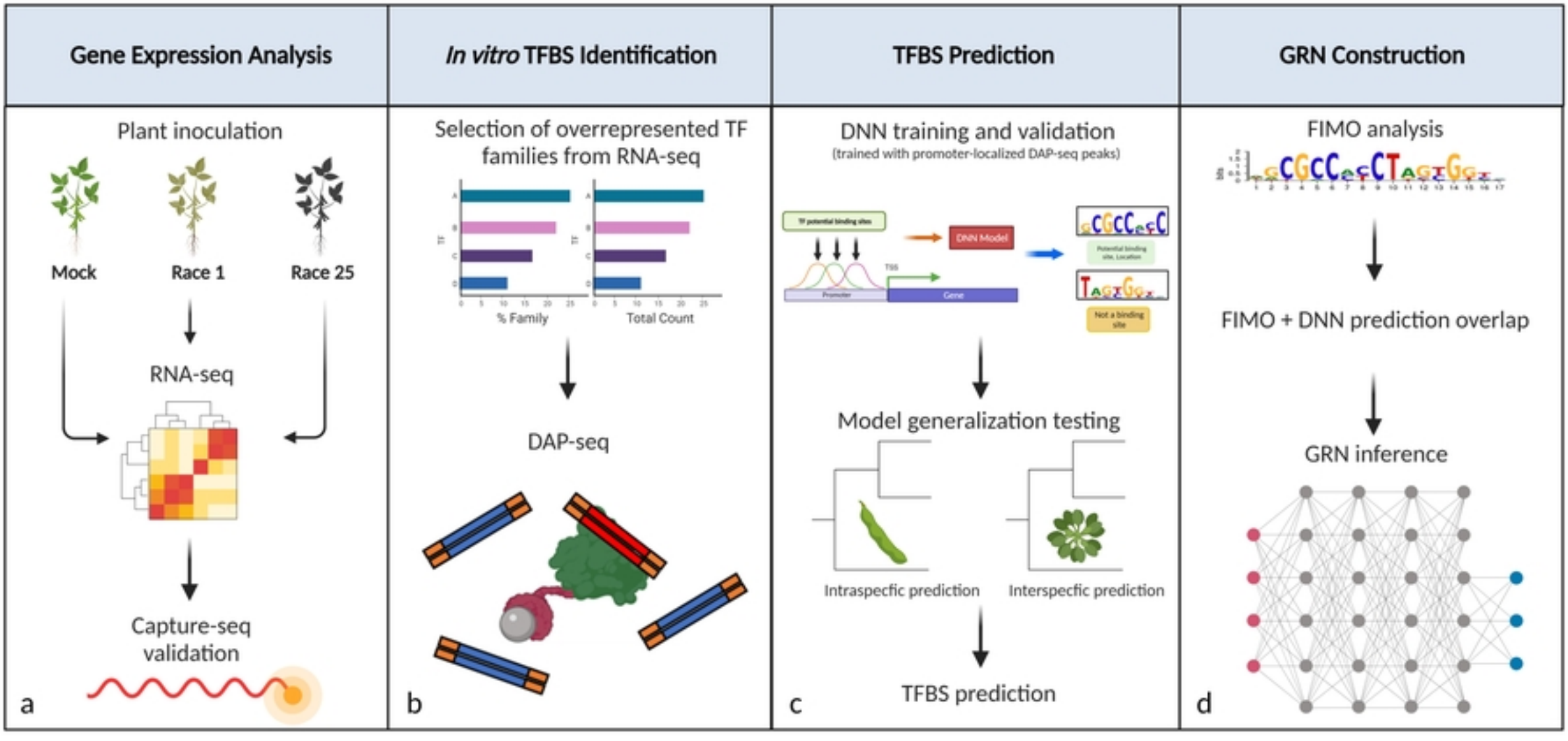
Gene Expression Analysis
Plant inoculation
Mock
Race 1
Race 25
RNA-seq
Capture-seq validation
a
In vitro TFBS Identification
Selection of overrepresented TF families from RNA-seq
% Family
Total Count
DAP-seq
b
TFBS Prediction
DNN training and validation
(trained with promoter-localized DAP-seq peaks)
DNN Model
Model generalization testing
Intraspecfic prediction
Interspecfic prediction
TFBS prediction
c
GRN Construction
FIMO analysis
FIMO + DNN prediction overlap
GRN inference
d

Figure 1

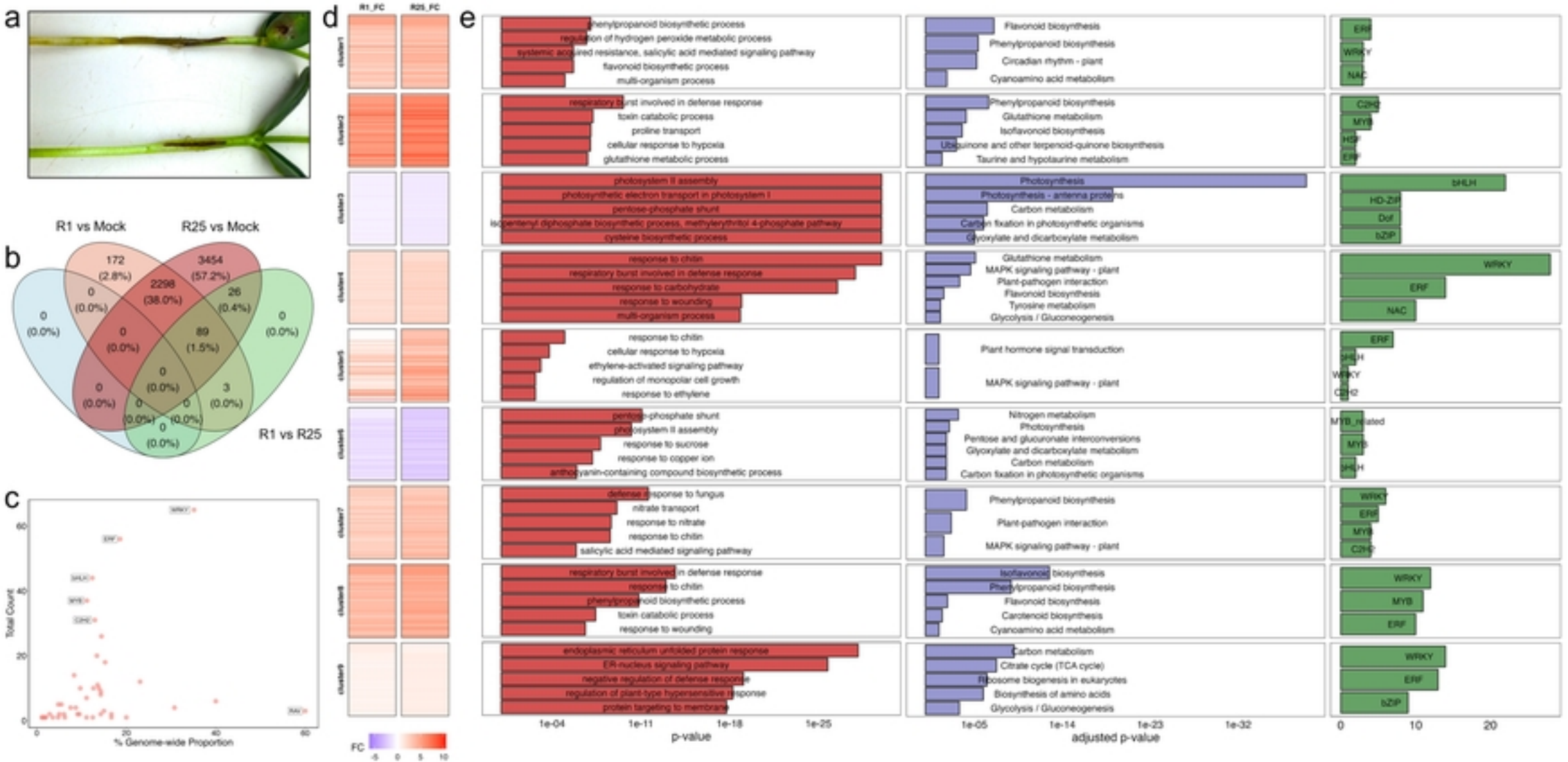
a
b
R1 vs Mock
R25 vs Mock
R1 vs R25
172 (2.8%)
3454 (57.2%)
2298 (38.0%)
26 (0.4%)
0 (0.0%)
89 (1.5%)
3 (0.0%)
c
Total Count
% Genome-wide Proportion
d
R1_FC
R25_FC
FC
e
Phenylpropanoid biosynthetic process
regulation of hydrogen peroxide metabolic process
systemic acquired resistance, salicylic acid mediated signaling pathway
flavonoid biosynthetic process
multi-organism process
Flavonoid biosynthesis
Phenylpropanoid biosynthesis
Circadian rhythm - plant
Cyanoamino acid metabolism
ERF
WRKY
NAC
respiratory burst involved in defense response
toxin catabolic process
proline transport
cellular response to hypoxia
glutathione metabolic process
Phenylpropanoid biosynthesis
Glutathione metabolism
Isoflavonoid biosynthesis
Ubiquinone and other terpenoid-quinone biosynthesis
Taurine and hypotaurine metabolism
C2H2
MYB
HSF
ERF
photosystem II assembly
photosynthetic electron transport in photosystem I
pentose-phosphate shunt
isopentenyl diphosphate biosynthetic process, methylerythritol 4-phosphate pathway
cysteine biosynthetic process
Photosynthesis
Photosynthesis - antenna proteins
Carbon metabolism
Carbon fixation in photosynthetic organisms
Glyoxylate and dicarboxylate metabolism
bHLH
HD-ZIP
Dof
bZIP
response to chitin
respiratory burst involved in defense response
response to carbohydrate
response to wounding
multi-organism process
Glutathione metabolism
MAPK signaling pathway - plant
Plant-pathogen interaction
Flavonoid biosynthesis
Tyrosine metabolism
Glycolysis / Gluconeogenesis
WRKY
ERF
NAC
response to chitin
cellular response to hypoxia
ethylene-activated signaling pathway
regulation of monopolar cell growth
response to ethylene
Plant hormone signal transduction
MAPK signaling pathway - plant
ERF
bHLH
WRKY
C2H2
pentose-phosphate shunt
photosystem II assembly
response to sucrose
response to copper ion
anthocyanin-containing compound biosynthetic process
Nitrogen metabolism
Photosynthesis
Pentose and glucuronate interconversions
Glyoxylate and dicarboxylate metabolism
Carbon metabolism
Carbon fixation in photosynthetic organisms
MYB_related
MYB
bHLH
defense response to fungus
nitrate transport
response to nitrate
response to chitin
salicylic acid mediated signaling pathway
Phenylpropanoid biosynthesis
Plant-pathogen interaction
MAPK signaling pathway - plant
WRKY
ERF
MYB
C2H2
respiratory burst involved in defense response
response to chitin
phenylpropanoid biosynthetic process
toxin catabolic process
response to wounding
Isoflavonoid biosynthesis
Phenylpropanoid biosynthesis
Flavonoid biosynthesis
Carotenoid biosynthesis
Cyanoamino acid metabolism
WRKY
MYB
ERF
endoplasmic reticulum unfolded protein response
ER-nucleus signaling pathway
negative regulation of defense response
regulation of plant-type hypersensitive response
protein targeting to membrane
Carbon metabolism
Citrate cycle (TCA cycle)
Ribosome biogenesis in eukaryotes
Biosynthesis of amino acids
Glycolysis / Gluconeogenesis
WRKY
ERF
bZIP
p-value
adjusted p-value

Figure 2

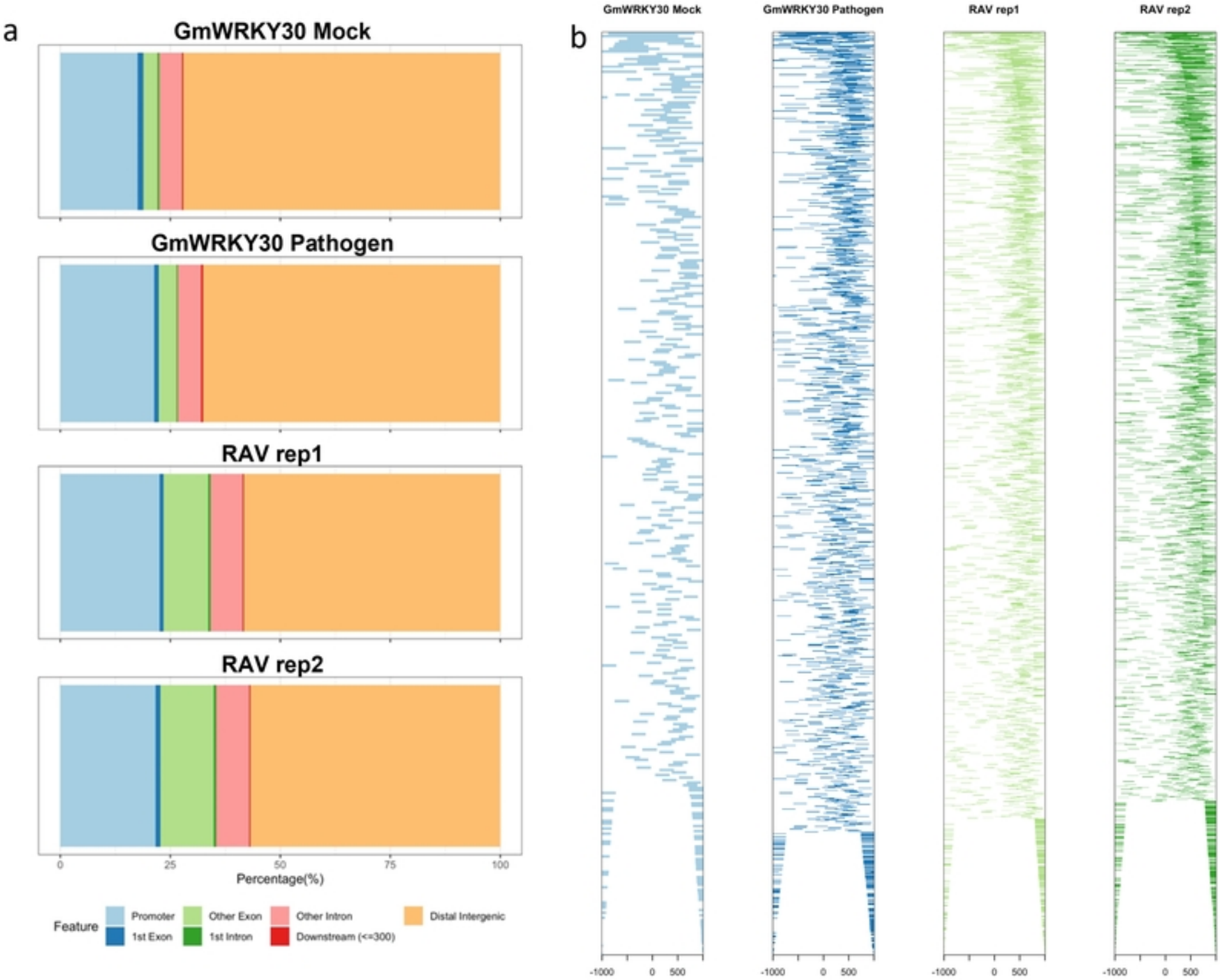
a
GmWRKY30 Mock
GmWRKY30 Pathogen
RAV rep1
RAV rep2
0
25
50
75
100
Percentage(%)
Feature
Promoter
1st Exon
Other Exon
1st Intron
Other Intron
Downstream (<=300)
Distal Intergenic
b
GmWRKY30 Mock
GmWRKY30 Pathogen
RAV rep1
RAV rep2
-1000
0
500

Figure 3

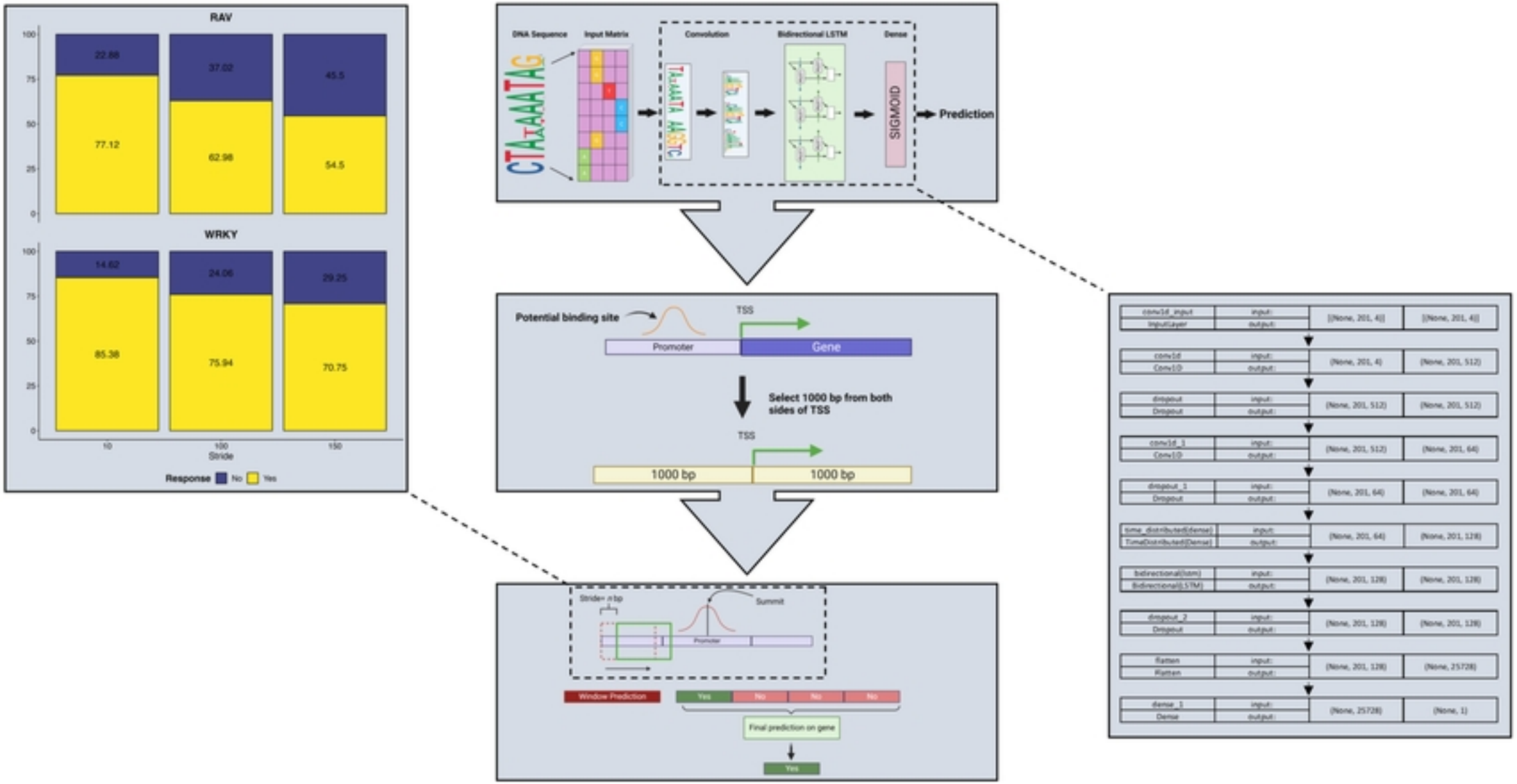
RAV
22.88
37.02
45.5
77.12
62.98
54.5
WRKY
14.62
24.06
29.25
85.38
75.94
70.75
Stride
Response
No
Yes
DNA Sequence
Input Matrix
Convolution
Bidirectional LSTM
Dense
SIGMOID
Prediction
Potential binding site
TSS
Promoter
Gene
Select 1000 bp from both sides of TSS
1000 bp
1000 bp
Summit
Window Prediction
Final prediction on gene

Figure 4

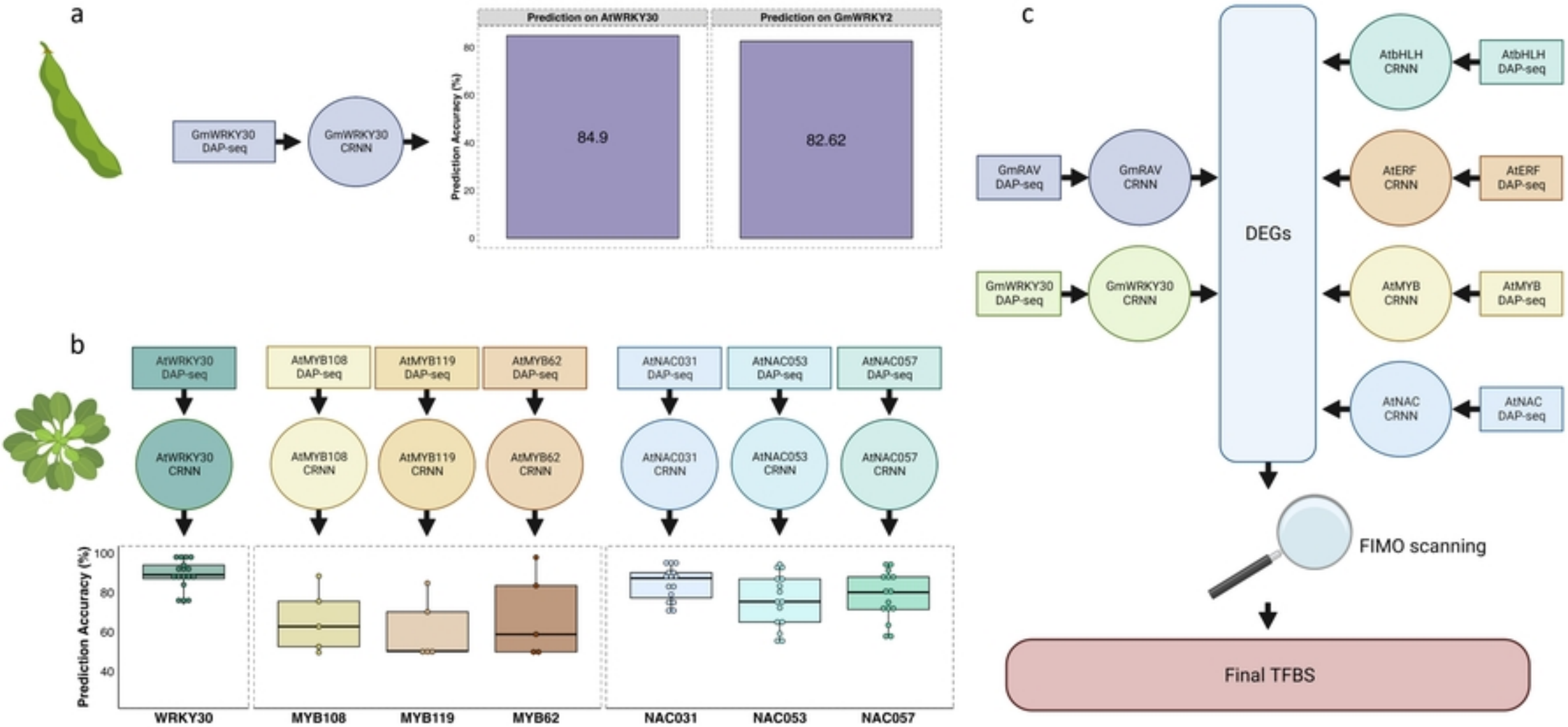
a
GmWRKY30 DAP-seq
GmWRKY30 CRNN
Prediction on AtWRKY30
Prediction on GmWRKY2
Prediction Accuracy (%)
84.9
82.62
b
AtWRKY30 DAP-seq
AtMYB108 DAP-seq
AtMYB119 DAP-seq
AtMYB62 DAP-seq
AtNAC031 DAP-seq
AtNAC053 DAP-seq
AtNAC057 DAP-seq
AtWRKY30 CRNN
AtMYB108 CRNN
AtMYB119 CRNN
AtMYB62 CRNN
AtNAC031 CRNN
AtNAC053 CRNN
AtNAC057 CRNN
Prediction Accuracy (%)
WRKY30
MYB108
MYB119
MYB62
NAC031
NAC053
NAC057
c
GmRAV DAP-seq
GmRAV CRNN
GmWRKY30 DAP-seq
GmWRKY30 CRNN
DEGs
AtbHLH CRNN
AtbHLH DAP-seq
AtERF CRNN
AtERF DAP-seq
AtMYB CRNN
AtMYB DAP-seq
AtNAC CRNN
AtNAC DAP-seq
FIMO scanning
Final TFBS

Figure 5

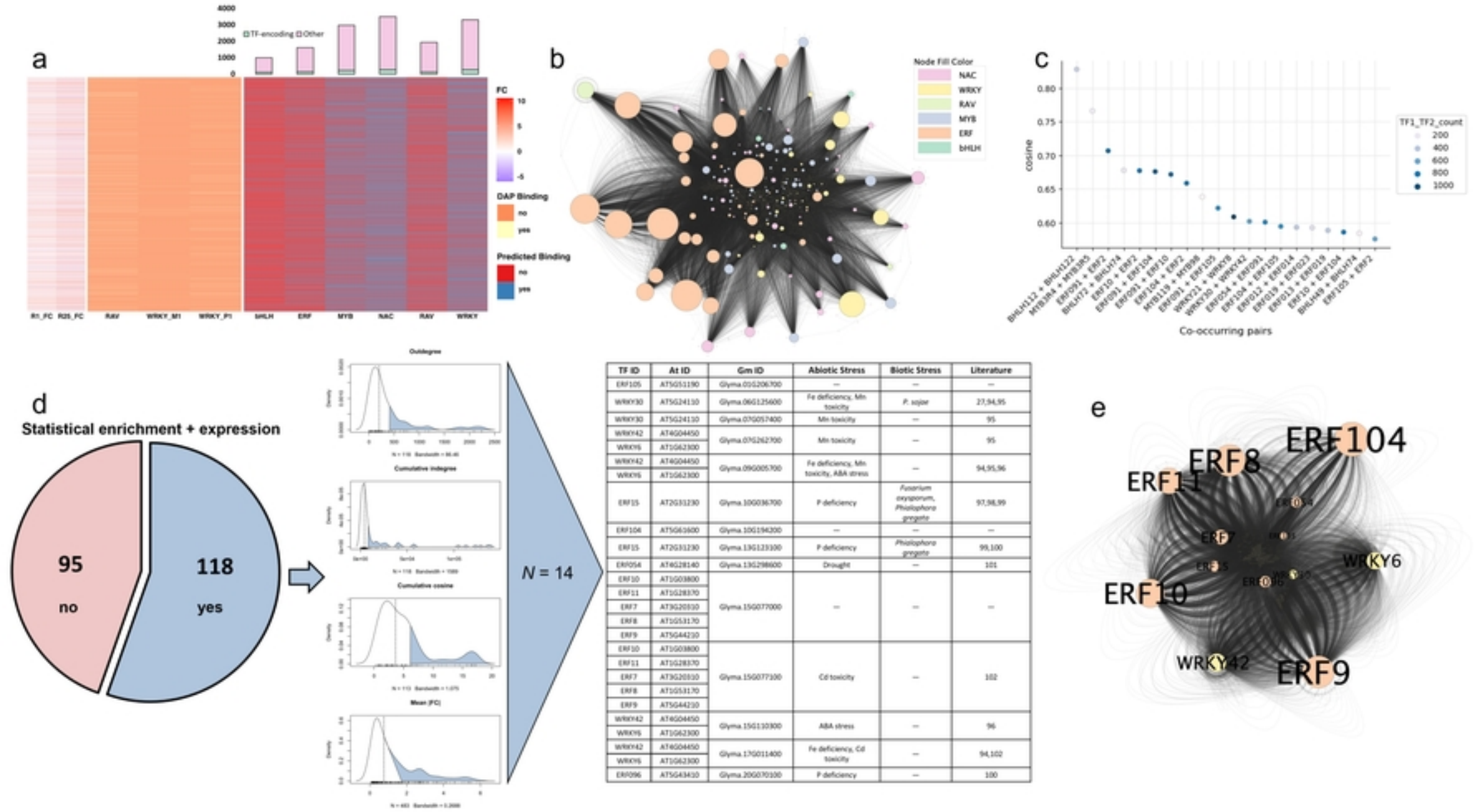

TF ID	At ID	Gm ID	Abiotic Stress	Biotic Stress	Literature
ERF105	AT5G51190	Glyma.01G206700	--	--	--
WRKY30	AT5G24130	Glyma.06G125600	Fe deficiency, Mn toxicity	*P. sojae*	27,94,95
WRKY30	AT5G24130	Glyma.07G057400	Mn toxicity	--	95
WRKY42	AT4G04450	Glyma.07G262700	Mn toxicity	--	95
WRKY6	AT1G62300				
WRKY42	AT4G04450	Glyma.09G005700	Fe deficiency, Mn toxicity, ABA stress	--	94,95,96
WRKY6	AT1G62300				
ERF15	AT2G31230	Glyma.10G036700	P deficiency	*Fusarium oxysporum*, *Phialophora gregata*	97,98,99
ERF104	AT5G61600	Glyma.10G194200	--	--	--
ERF15	AT2G31230	Glyma.13G123100	P deficiency	*Phialophora gregata*	99,100
ERF054	AT4G28140	Glyma.13G298600	Drought	--	101
ERF10	AT1G03800	Glyma.15G077000	--	--	--
ERF11	AT1G28370				
ERF7	AT3G20810				
ERF8	AT1G53170				
ERF9	AT5G44230				
ERF10	AT1G03800	Glyma.15G077100	Cd toxicity	--	102
ERF11	AT1G28370				
ERF7	AT3G20810				
ERF8	AT1G53170				
ERF9	AT5G44230				
WRKY42	AT4G04450	Glyma.15G130300	ABA stress	--	96
WRKY6	AT1G62300				
WRKY42	AT4G04450	Glyma.17G011400	Fe deficiency, Cd toxicity	--	94,102
WRKY6	AT1G62300				
ERF096	AT5G43410	Glyma.20G070100	P deficiency	--	100

Figure 6